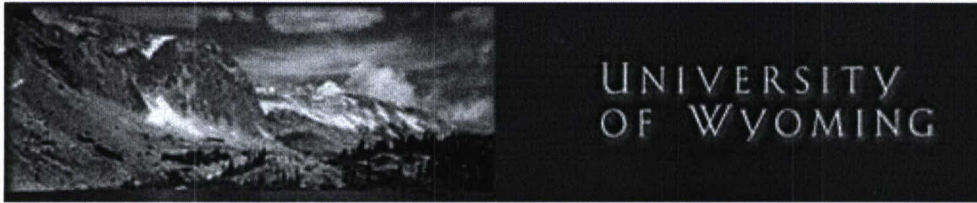


REPORT DOCUMENTATION PAGE				Form Approved OMB No. 0704-0188	
Public reporting burden for this collection of information is estimated to average 1 hour per response, including the time for reviewing instructions, searching existing data sources, gathering and maintaining the data needed, and completing and reviewing this collection of information. Send comments regarding this burden estimate or any other aspect of this collection of information, including suggestions for reducing this burden to Department of Defense, Washington Headquarters Services, Directorate for Information Operations and Reports (0704-0188), 1215 Jefferson Davis Highway, Suite 1204, Arlington, VA 22202-4302. Respondents should be aware that notwithstanding any other provision of law, no person shall be subject to any penalty for failing to comply with a collection of information if it does not display a currently valid OMB control number. PLEASE DO NOT RETURN YOUR FORM TO THE ABOVE ADDRESS.					
1. REPORT DATE (DD-MM-YYYY) 13-12-2006		2. REPORT TYPE Final		3. DATES COVERED (From - To) 06/15/03-09/14/06	
4. TITLE AND SUBTITLE Active Flutter Suppression Using Cooperative, High Frequency, Dynamic Resonant Aero-Effectors				5a. CONTRACT NUMBER	
				5b. GRANT NUMBER F49620-03-1-0358	
				5c. PROGRAM ELEMENT NUMBER	
6. AUTHOR(S) Jonathan Naughton William Lindberg John McInroy				5d. PROJECT NUMBER	
				5e. TASK NUMBER	
				5f. WORK UNIT NUMBER	
7. PERFORMING ORGANIZATION NAME(S) AND ADDRESS(ES) University of Wyoming Dept. 3295 1000 E. University Avenue Laramie, WY 82071				8. PERFORMING ORGANIZATION REPORT NUMBER UWAA-2006-2	
9. SPONSORING / MONITORING AGENCY NAME(S) AND ADDRESS(ES) Air Force Office of Scientific Research 801 N. Randolph Street Arlington, VA 22203 <i>Dr Victor Giurgintu/NA</i>				10. SPONSOR/MONITOR'S ACRONYM(S) AFOSR	
				11. SPONSOR/MONITOR'S REPORT NUMBER(S)	
12. DISTRIBUTION / AVAILABILITY STATEMENT Approved for public release; distribution unlimited.					
13. SUPPLEMENTARY NOTES					
14. ABSTRACT An investigation of the use of actuators that cause aerodynamic disturbances that could be used for flutter control was investigated. Flutter control requires large disturbances to produce the aerodynamic loads needed to oppose the flutter forces. As a result, oscillating fence actuators that have low power consumption and high control authority that scales with flight speed were studied. These fence actuators were tested in laminar and turbulent boundary layers to characterize the disturbances they produced. They have also recently been studied on a two-dimensional airfoil. By modeling the disturbances produced by these actuators, control modeling indicated that they could be used to dampen flutter-like motion. As a result of these initial findings, it is concluded that the use of such actuators for flutter controls is promising and should be investigated further.					
15. SUBJECT TERMS					
16. SECURITY CLASSIFICATION OF: UNCLASSIFIED			17. LIMITATION OF ABSTRACT UL	18. NUMBER OF PAGES	19a. NAME OF RESPONSIBLE PERSON
a. REPORT UNCLASSIFIED	b. ABSTRACT UNCLASSIFIED	c. THIS PAGE UNCLASSIFIED			19b. TELEPHONE NUMBER (include area code)

AFRL-SR-AR-TR-07-0064



UWAA-2006-2

• • • • •

Active Flutter Suppression Using Cooperative, High Frequency, Dynamic-Resonant Aero-Effectors

DISTRIBUTION STATEMENT A

Approved for Public Release
Distribution Unlimited

Final Report

*William D. Armstrong, Willam R. Lindberg, John E.
McInroy, and Jonathan W. Naughton*

For the period June 15, 2003 – September 15, 2006

F49620-03-1-0358

Introduction

Active suppression of aeroelastic flutter and gust loading promises to strongly increase the efficiency and performance of military and non-military aircraft. Increases in efficiency are primarily expected from the reduction of structural margin and therefore from the reduction of aircraft empty weight that may then be used to increase aircraft payload, range, or maneuvering performance. These issues are of particular concern in high performance fighters, UAVs, and missiles where great need exists for simultaneously increasing range and payload without decreasing maneuvering performance.

Conventional active vibration control and flutter suppression systems are servo-hydraulic. Conventional servo-hydraulic technology is burdened by a set of undesirable characteristics that effectively restrict their use to large aircraft. The servo-hydraulic based systems have multiple critical parts and are therefore susceptible to multiple point failures. The hydraulic servo valves, pumps and pipe networks are very heavy. The compressibility of the hydraulic fluid, viscous losses in the moving hydraulic fluid and bandwidth limitations in the servo-valves themselves limit these systems to relatively low frequency applications (Giurgiutiu, 1995).

Small-scale active materials based systems do not suffer many of the deficiencies of the servo-hydraulic systems. They directly connect displacement with electrical energy, and therefore they tend to have relatively few failure points. They are very lightweight. The active parts of the system may be made small and therefore many individual effectors may be distributed across an area providing high system redundancy. Perhaps most importantly, these types of devices have inherently high frequency bandwidth and therefore may effectively operate to reduce vibration and flutter in small, stiff high frequency aero-structures outside of the range of conventional servo-hydraulic systems. Although actively-controlled material systems have shown promise, they consume large amounts of energy, require heavy power supplies, are very expensive, fragile and have limited stiffening capability. In this study, a new and potentially more effective dynamic-resonant approach is studied where the aerodynamic control forcing comes from a distributed set of high frequency dynamic-resonant effectors. The aero-effector displacement is amplified locally by operating the device in resonance. We expect that this form of complex active system results in minimum weight and power and low maximum voltage requirements. These systems are therefore of particular interest for small, relatively high modal frequency, high performance aircraft such as fighters, UAVs, missiles and light business jets, and for particularly demanding flight regimes such as high g onset and accelerated flight with unbalanced stores configurations.

Our proposed method is ultimately based on the high frequency control of boundary layers. Control of boundary layers, typically to prevent separation, has been extensively studied for nearly a century (see the review articles by Bushnell and McGinley 1989 and Fiedler and Frenholz 1990 for examples). Specifically, this study has investigated the generation of periodic disturbances in the boundary layer. Interest in periodic excitation has grown due to the reduction in the momentum injection or the energy required to produce the desired control. Periodic systems can require up to an order of magnitude less energy than their "steady" counterparts (Greenblatt and Wygnanski 2000). Such gains are obviously of interest to operational aircraft.

Although periodic disturbance actuators studied in the past have produced satisfactory results in several flows, the demands for flutter control are somewhat different than those of past applications for such actuators. In particular, large disturbances capable of significant changes in the local pressure coefficient are required. In addition, the disturbance must be able to scale with flight velocity since many of the applications may be in the transonic

regime where many periodic actuation devices struggle to produce a sufficient disturbance. As a result, the work here focused on actuators that harness energy from the flow itself rather than trying to produce it themselves. The actuators that were determined to best fit the needs of flutter control were oscillating fence actuators. Such actuators should produce disturbance on the scale of the fence, be capable of high frequency operation, consume little power, and produce disturbance levels that increase with flight velocity. Unfortunately, these actuators have received little attention in the past, and, as a result, a large portion of the effort in this study was spent characterizing these actuators and the disturbances they produce as well as reasoning how they would be used to control the flow.

The remainder of this report is organized into the topical areas that have been investigated: oscillating fence flows physics, resonant fence actuator disturbance characterization, resonant fence actuator used on an airfoil, and control issues for actuators on a fluttering wing. Ongoing and future work is also suggested in light of what has been accomplished in this effort.

Oscillating Fence Flow Physics

This portion of the work was an experimental examination of the fundamental features of the flows that are generated by the presence of oscillatory fences embedded within laminar boundary layers. Further details of the results presented here may be found in Singh 2005.

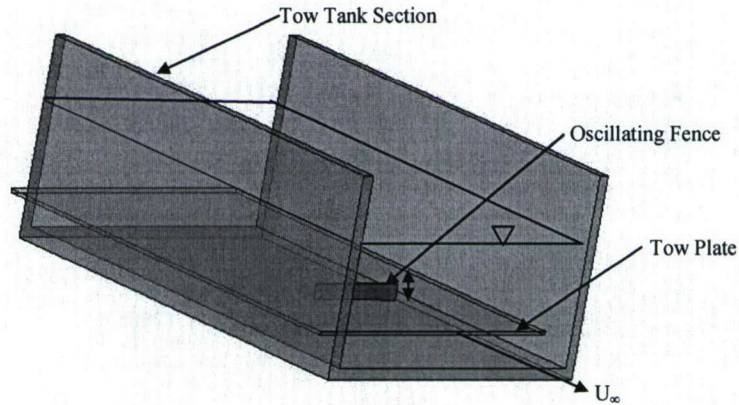


Figure 1 - Schematic diagram of oscillating fence geometry in water tow tank.

Experimental Apparatus

A water tow tank was used for the study. A simplified schematic of the oscillating fence and tow plate system is given in Figure 1. The tow tank is 9 m long, with a cross-section of 30 cm wide by 20 cm high. The plate tow speeds (i.e. free-stream velocities) were varied between 2 and 5 cm/s. The maximum height of the fence is 1.27 cm, the width of the fence is 3.81 cm and the thickness of the fence is 0.50 cm. The fence is located 90 cm downstream from the leading edge. The tow-plate dimensions are 190 cm in length, 20 cm in width and 0.3 cm in thickness. The maximum Reynolds number, Re_x , based on the distance from the leading edge to the fence location is 6×10^4 , which justifies the experimental observation that the boundary layer at the fence location was laminar. The theoretical laminar boundary layer thickness at

the fence location was calculated from the Blasius solution, and varied from 2.14 cm to 3.45 cm. Flow visualization was by Sodium Fluorescence dye injection, and the resulting streaklines were illuminated with a 1 cm wide light sheet. The flow patterns were then recorded on digital video. Subsequent analysis of the digital video involved image processing to enhance the images and identifying flow structures, their evolution and dimensions.

The oscillating fence motion was generated by a variable speed DC motor that drove a Scotch yoke mechanism, thus providing a true sinusoidal motion,

$$\frac{y}{h/2} = 1 - \cos(2\pi f_o t),$$

where f_o is the fence height oscillation frequency, $y(t)$ and h are the fence height and maximum fence heights, respectively.

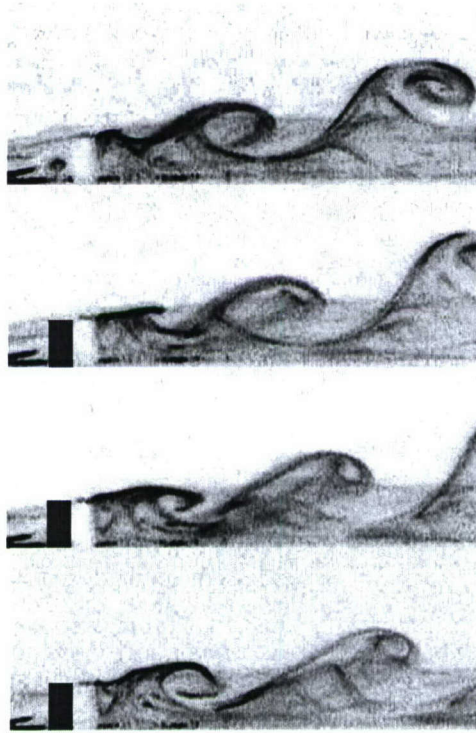


Figure 2 - Sequential images of vortex shedding behind a stationary fence. The cycle time, t , is initialized at the instant of the prior vortex release. The subsequent times are non-dimensionalized by the shedding frequency, f_s (Hz), so the sequence corresponds to ft values of 0.25, 0.50, 0.75 and 1.0, respectively. Experimental parameters are: $Re_h = 254$, $h/w = 0.33$, $h/\delta = 0.37$ (as calculated by the Blasius solution).

Results

Stationary Fence

Initially, a series of tests were done on a stationary fence that projected a distance, h , out into the flow. Figure 2 illustrates the type of vortical structures that are generated by this type of flow (the illumination is upon the center of the fence) where the evolution of a vortex over the generation and shedding cycle are shown. Over the range of fence Reynolds numbers examined ($254 < Re_h < 635$, where $Re_h = U_\infty h/\nu$), these vortices are observed to be quite stable,

repeatable and initially are of the same dimension as the fence. Subsequent tracking of these structures indicate that they diminish in strength and are differentially advected by the boundary layer flow.

Shedding frequencies were easily determined from the image sequence. The shedding frequency downstream of the stationary fence was measured as a function of the free-stream velocity, U_∞ , and the fence height, h . In this circumstance, a Strouhal number may be defined:

$$St_s = \frac{f_s h}{U_\infty},$$

where f_s is the shedding frequency (in Hz). Figure 3 summarizes the stationary fence shedding frequency results.

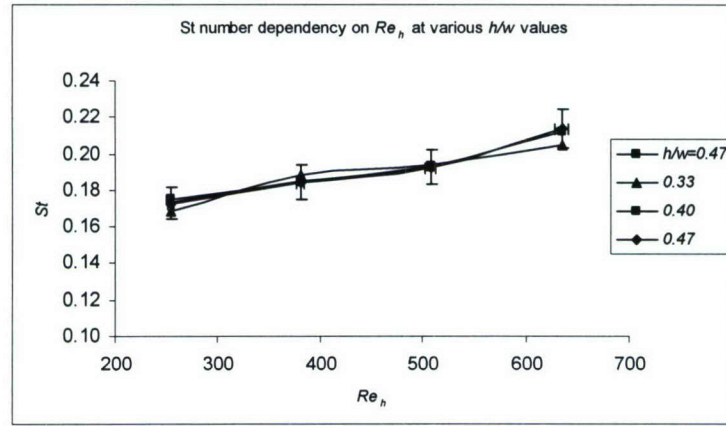


Figure 3 - Strouhal number (St) as a function of Reynolds number, Re_h , and aspect ratio, h/w , for a static fence. The width, w , of the fence was held constant at $w = 3.81\text{cm}$. The estimates of the errors are: $\pm 5\%$ in St and $\pm 1\%$ in Re_h (error bars are shown for $h/w=0.47$).

Over the limited range of Reynolds numbers of these experiments, St_s was found to be a weak function of Re_h , where a regression analysis indicates:

$$St_s \sim 0.15 + 9.10^{-5} * Re_h (\pm 5\%).$$

This weak dependence on Re_h may be attributed to the dependence of St on the ratio, (h/δ) , where δ is the boundary layer thickness at the fence location. Whether the increase in Re_h is due to an increase in free-stream velocity, U_∞ (i.e. smaller δ), or fence height, the net result is the top of the fence is higher in the boundary layer and experiences a higher net velocity. Over the range of fence width ratios that were studied ($h/w \sim 0.27$ to 0.47 , where w is the fence width), the Strouhal number remained unchanged (for constant Re_h). A vortex advection speed, U_a , was easily calculated from the digital images by tracking identifiable features of the vortex over the range of the image. The initial advection velocities, as expressed non-dimensionally as U_a/U_∞ , remained constant over the experimental range of Re_h :

$$U_a/U_\infty = 0.65.$$

As a first approximation, it has been suggested¹² that vortex shedding is characterized by a vortex strength, K . Additionally, the advection velocity ratio (for a vortex in an inviscid fluid adjacent to a boundary) is proportional to the vortex strength¹³:

$$U_a/U_\infty \approx 1 - K/4\pi h U_\infty,$$

so the observed constancy of U_a/U_∞ is consistent with this simple model if $K \sim h U_\infty$ (or Re_h).

Oscillating Fence

A non-dimensional oscillating fence frequency may then be defined, based on the corresponding shedding frequency of the static fence, f_s (at the same Reynolds number. Based on the maximum height of the fence, h):

$$\phi_o = f_o/f_s,$$

where f_o is the oscillation frequency of the fence. Based on the observed behavior of the flow, four different flow regimes as a function of relative frequency have been identified:

1. Critical Zone [$\phi_o \sim O(1)$],
2. Sub-critical Zone [$\phi_o < 0.1$],
3. Transitional Zone [$\phi_o \sim 0.1 - O(1)$], and
4. Supercritical Zone [$\phi_o > O(1)$].

We shall discuss the four regime behaviors separately; however there is one overriding theme: the intrinsic frequency of each of these coherent flow regimes (i.e. all but the transitional zone) is the same as the shedding frequency of the flow over a static fence.

1. Critical Zone [$\phi_o \sim O(1)$]: There is one stable vortex shed per oscillation of the fence. The characteristics of the vortex are very similar to the flow structure of the static fence at the same Re_h . Hence, St_o and U_a/U_∞ are essentially equal to the corresponding static fence values (at the same Re_h). A sequence of images over an oscillation cycle is shown in Figure 4. One noticeable difference between the stationary and oscillating fence structures (Figure 2 and Figure 4) is the stronger vortex straining in the case of the oscillation fence, due to the exposure of the vortex to more of the boundary layer velocity gradient over portions of the cycle (i.e. small y/h). Penetration of these structures into the flow is reduced over the static case.
2. Sub-critical Zone [$\phi_o < 0.1$]: The motion of the fence is sufficiently slow that the motion may be considered “quasi-steady”, where, over a significant fraction of the oscillation cycle, vortices are shed at the shedding frequency appropriate to the average Reynolds number over the shedding cycle. The vortices that are produced are stable, but their spacing is variable, depending on the part of the fence height cycle that the vortex is produced. An approximate lower limit on vortex shedding may be made for the case of small ϕ_o , where for values of $Re_y \approx 65$ (or less), no vortices are observed to form. These multiple vortices are not observed to interact with each other.
3. Transitional Zone [$\phi_o \sim 0.1 - O(1)$]: In this regime, one vortex is observed to be shed per fence oscillation. The shed vortex is unstable and breaks down to turbulent structures within a few fence heights downstream, as is shown in Figure 5.
4. Supercritical Zone [$\phi_o > 1$]: At these higher fence oscillation frequencies, one vortex is generated per oscillation of the fence. These vortices are significantly smaller than the maximum fence height, h (in contrast to either the static fence or $\phi_o = 1$ vortex structures). These smaller vortices are observed to coalesce downstream, forming a larger, stable vortex. Over many fence oscillations, on average, ϕ_o vortices coalesce

to form one vortex. An example sequence showing this “pairing” behavior is shown in Figure 6, for $\phi_0 = 4$.

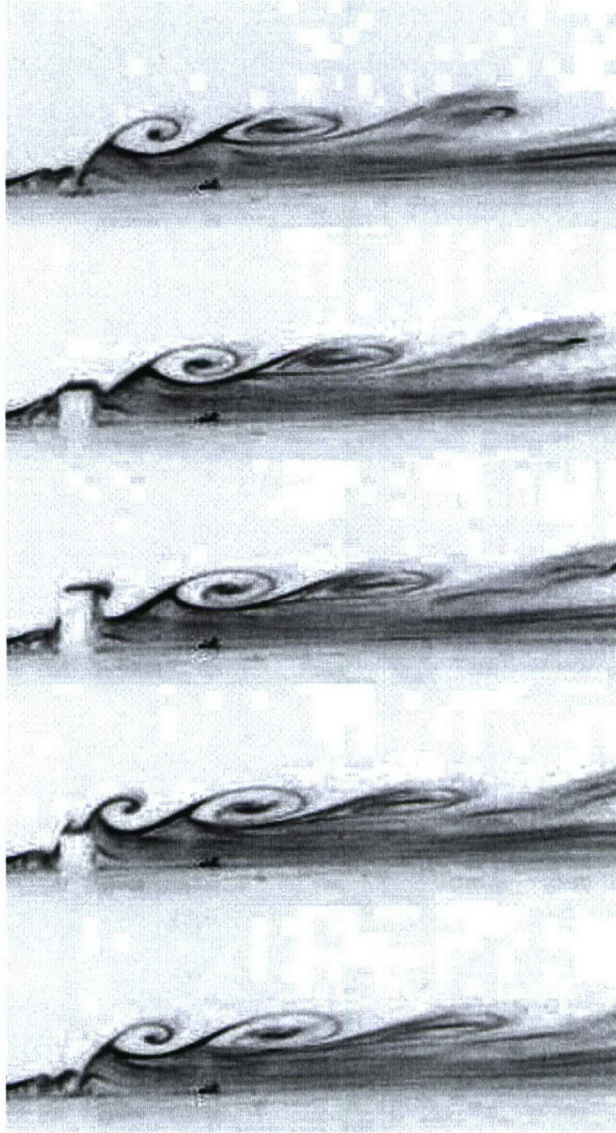


Figure 4 - Vortex formation and shedding at $\phi_0 \sim 1$ (critical) and $Re_h = 254$ at $y = h/2$ intervals, starting at $h = 0$ (note that the sequence is based on y/h , not ft , so the time intervals between frames is not constant).

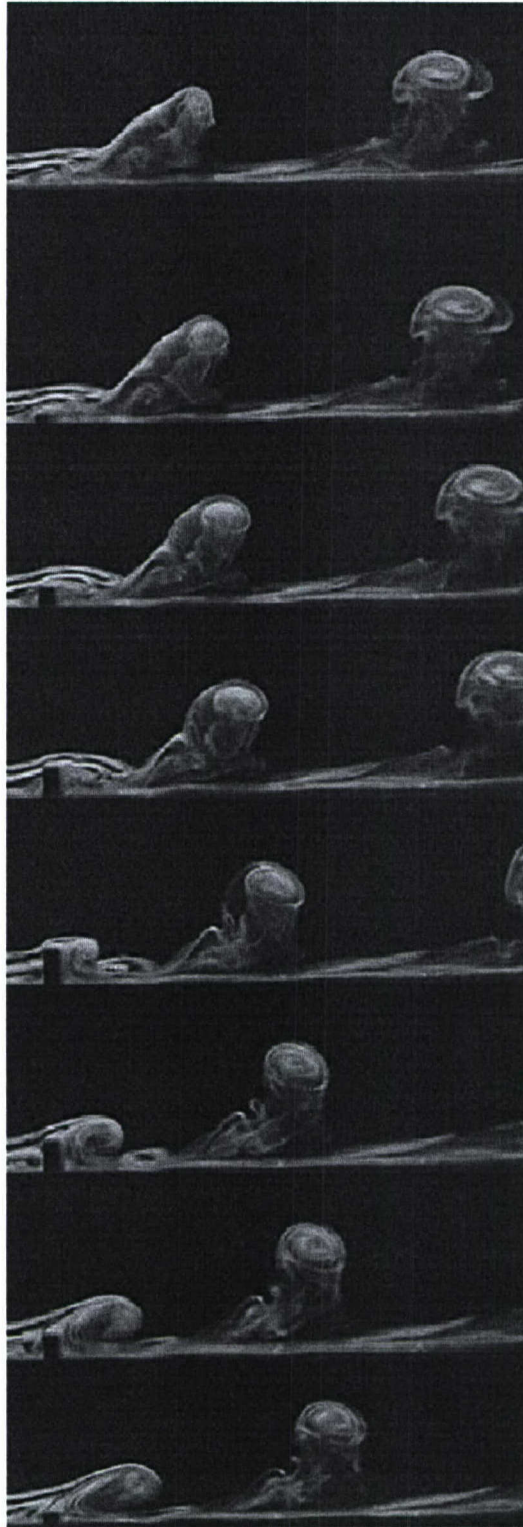


Figure 5 - Transitional zone flow structures for $\phi_0 = 0.375$ and $Re_h = 254$. The images are shown at y/h increments of 0.25 (ascending and descending), starting at $y/h = 0$.

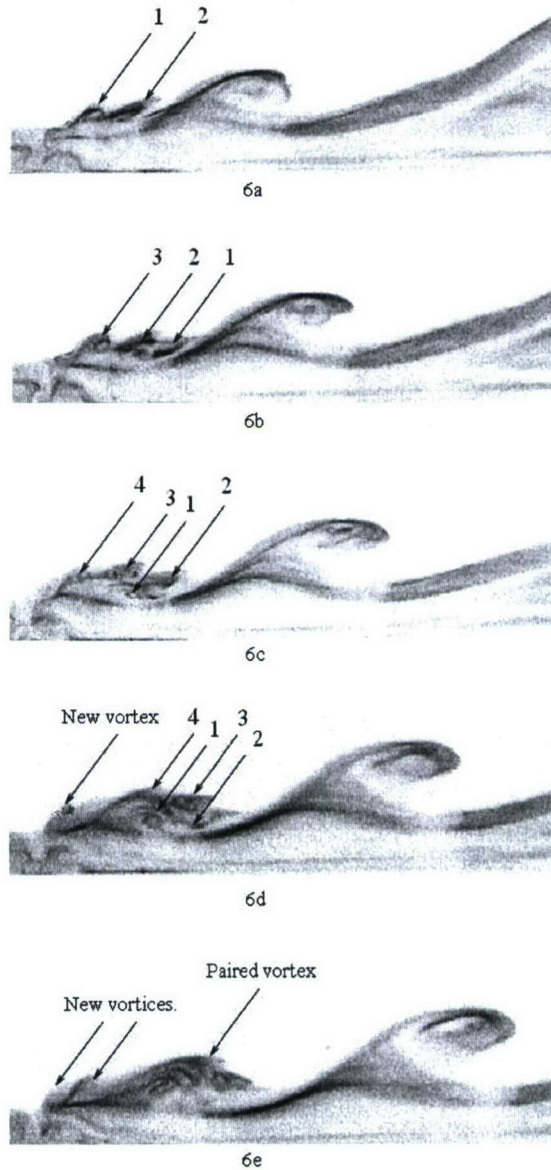


Figure 6 - Vortex shedding and pairing at $\phi_o = 4$ and $Re_h = 254$. Four vortices are observed to coalesce to form a final, stable vortex. Individual vortices are labeled 1-4, representing the vortex shed at fence oscillation 1 through 4. For each of the frames, the fence is at the bottom of its travel.

Based on the final frequency of generation of the final vortices, St values correspond closely to the static fence results (although slightly less), as is shown in Figure 7. We note that there is a slight decrease in St for higher values of ϕ_o , particularly the non-integer values of ϕ_o . Such a decrease in St may be attributed to the occasional “orphan” vortex that is not incorporated into the larger vortex. The corresponding advection speed ratio of the coalesced vortices is shown in Figure 8, where there is observed a slight increase in advection speed at the higher values of ϕ_o , where the dissipation associated with the vortex interactions would decrease the vortex strength, resulting in an increase in advection velocity for a given Re_h .

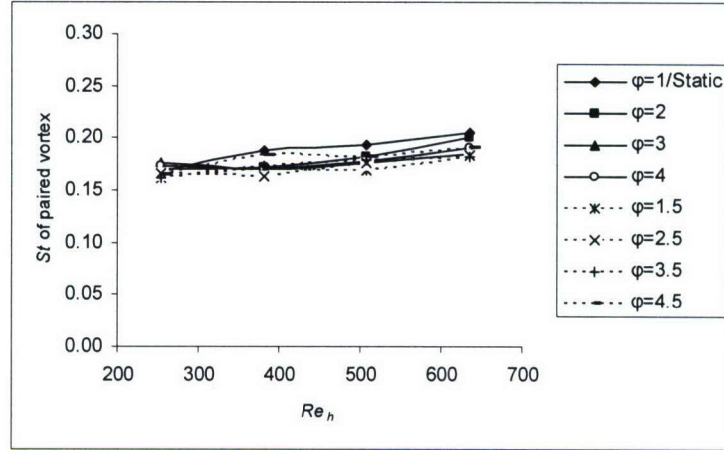


Figure 7 - Strouhal number of final, coalesced stable vortices at various frequency ratios, ϕ_o .

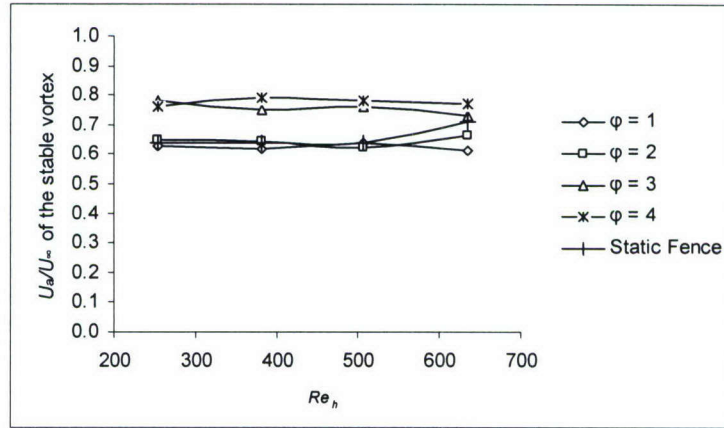


Figure 8 - Normalized vortex convection speed of coalesced vortices at various frequency ratios, ϕ_o .

A table summarizing the characteristics of the vortices produced at different frequency ratios is shown in Table 1.

Table 1 – Summary of vortex characteristics at different frequency ratios.

	$\phi_o = 0$ (static)	$\phi_o < \sim 0.1$ (sub-critical)	$0.1 < \phi_o < O(1)$ (transitional)	$\phi_o \sim O(1)$ (critical)	$\phi_o > O(1)$ (super-critical)
Primary Vortex	Coherent	Coherent	Three-dimensional, unstable	Coherent	Vortex-pairing
Horse-shoe Vortex	Present	Present most of the time.	Non-stationary presence	Non-stationary presence	Absent
St	~ 0.2	~ 0.15	NA	~ 0.2	~ 0.2
U_v/U_∞	~ 0.65	~ 0.65	NA	~ 0.65	> 0.65

Ongoing Work

The flow visualization studies just presented have been very revealing of the flow structures generated by oscillating fences. However, the study did not provide actual velocity fields.

Therefore, such quantities of interest as the interaction and decay of vortices originating at the fence as well as quantitative measurements of vortex advection speed and strength could not be determined. The very distinct differences in the flow behavior between laminar and turbulent boundary layer/fence interactions are also of interest. The flow visualization showed a natural shedding frequency for the static fence in a laminar flat plate boundary layer, whereas a natural shedding frequency was not observed in the static fence wind tunnel studies in a turbulent flat plate boundary layer (Medina, et al, 2006).

Two-dimensional Particle Image Velocimetry (PIV) is currently being used to quantify the velocity field of static and oscillating fences in a laminar flat plate boundary layer. The velocity fields for this flow situation are being measured in the same tow tank used in the flow visualization studies, with the PIV system used for the flat plate turbulent boundary layer case of static and oscillating fences in a wind tunnel (Medina, et. al. 2006). The Nd:YAG laser is mounted in a stationary position at the upstream end of the tow tank. The light sheet is produced by redirecting the laser beam through two Newport high energy mirrors, to the LaVision sheet optics, all of which are mounted on the tow tank carriage. The tow tank is seeded with Potters Industries Inc. ~11 micron diameter SPHERICEL® hollow glass spheres. The light sheet illuminated an x-y cross section of approximately 50mm x 35mm. The flow velocities were calculated via cross-correlation using multi-pass decreasing window size technique. All initial data sets shown were taken with a carriage velocity of 5 cm/s.

The first data set of interest is that of the flat plate boundary layer in the absence of the fence. This experiment is used to ensure that the boundary layer is laminar and well-conditioned. Figure 9 shows the mean x velocity component for the fenceless boundary layer.

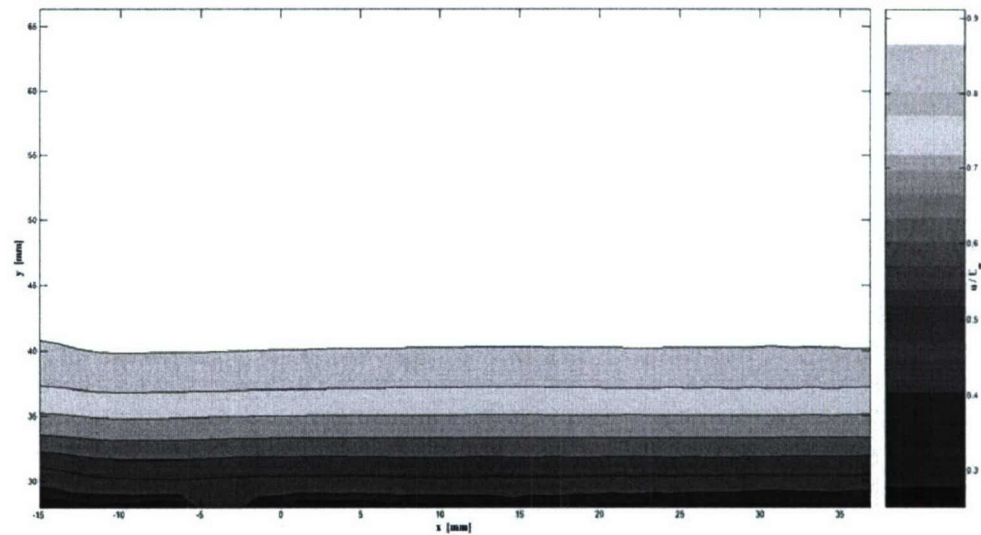


Figure 9 - PIV mean x-velocity component (u/U_{∞}) for the fenceless flat plate boundary layer ($U_{\infty} \sim 5$ cm/s, $Re_x \sim 50,000$). The mean velocities were calculated from 720 PIV images.

Figure 9 shows a u velocity disturbance near the plate surface at $-6 < x < 0$ mm. This disturbance is due to suction through the fence slit ($x \sim -3$ mm) due to a pressure difference between the top and bottom of the plate. This suction effect is more evident in the v velocity near the fence slit, as is shown in Figure 10.

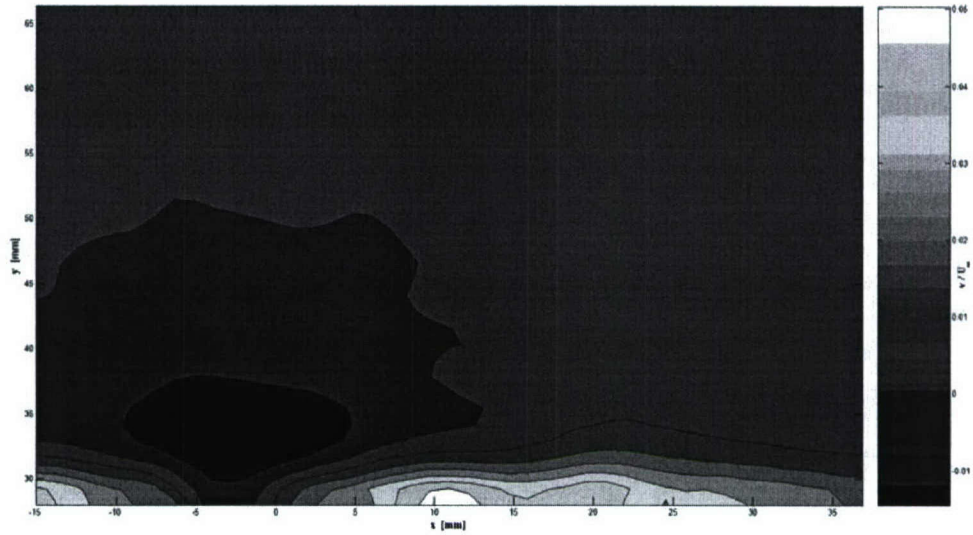


Figure 10 - PIV mean y-velocity component (v/U_x) for the fenceless flat plate boundary layer ($U_\infty \sim 5$ cm/s, $Re_x \sim 50,000$) to demonstrate the suction through fence slit ($x \sim -3$ mm) due to a pressure difference between top and bottom of plate. The mean velocities were calculated from 720 PIV images.

Though the pressure difference across the plate is significant (as evident from the apparent suction in Figure 10), the disturbances do not appear to drastically affect the boundary layer. Figure 11 shows that the experimental data at locations upstream and downstream of the slot ($x \sim -15$ mm and 37mm) along with the Blasius laminar boundary layer solution. It is evident from the figure that the velocity profile at both of these locations is closely approximated by the Blasius solution.

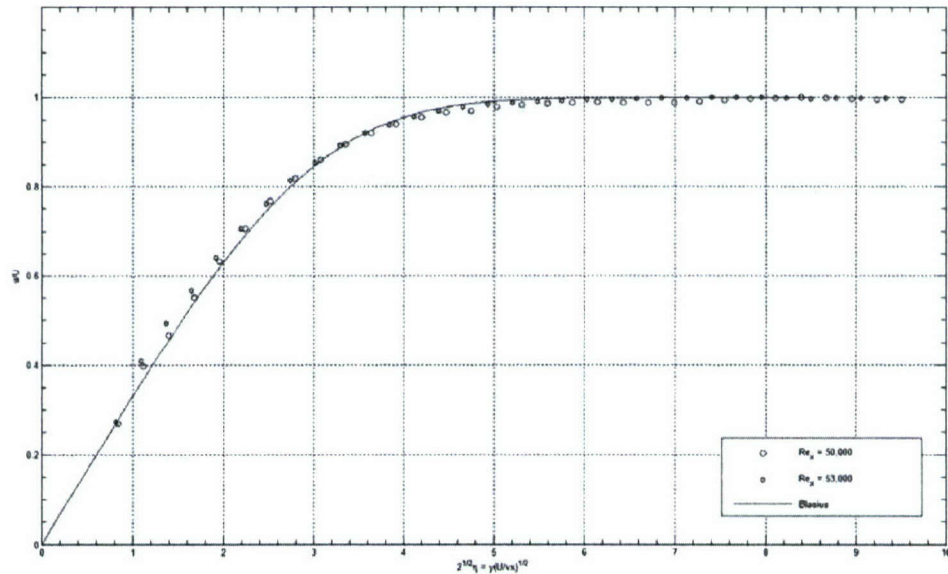


Figure 11 - Blasius velocity profiles ahead of and ($x \sim -15$ mm and 37mm, $Re_x = 50,000$ and 53,000) for the fenceless flat plate boundary layer.

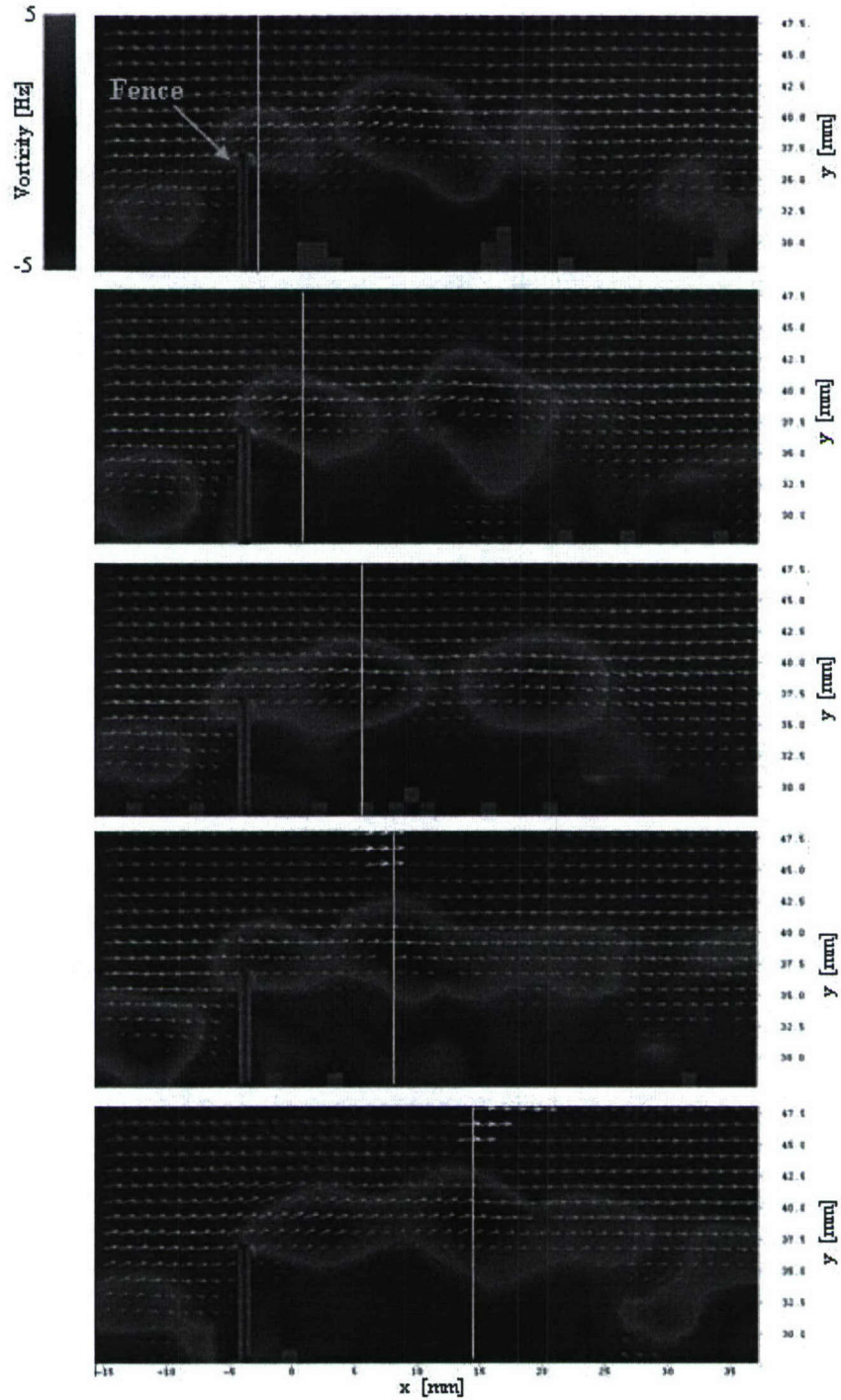


Figure 12 - Sequential velocity and vorticity fields (from PIV images) of vortex shedding downstream of a static fence in a laminar flat plate boundary layer at $U_\infty \sim 5$ cm/s, $Re_x \sim 50,000$, $Re_h \sim 640$, and a fence height of 1.27 cm. Images sampled at ~ 5 Hz.

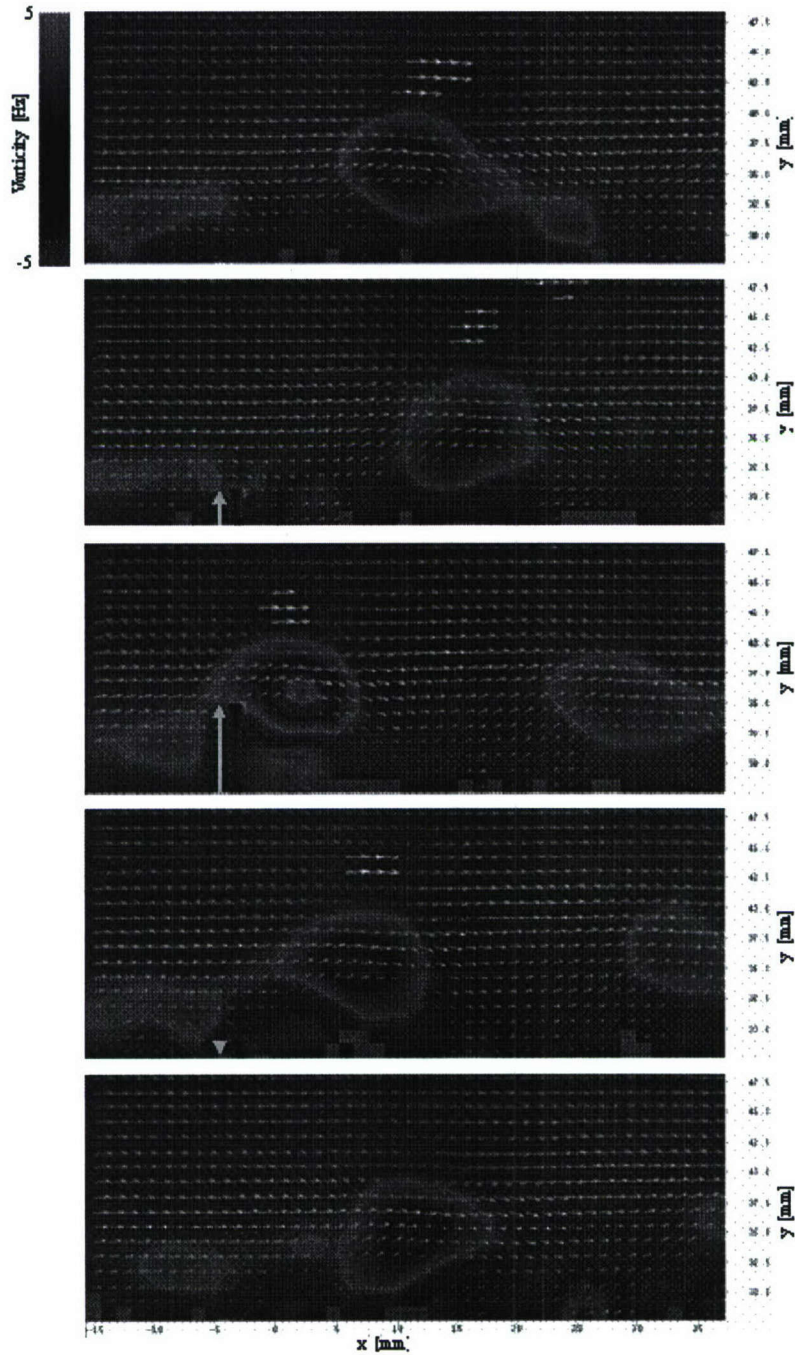


Figure 13 - Sequential velocity and vorticity fields (from PIV images) for one fence cycle of vortex shedding downstream of a 1 Hz oscillating fence in a laminar flat plate boundary layer at $U_\infty \sim 5$ cm/s, $Re_x \sim 50,000$, $Re_h \sim 640$, and a maximum fence height of 1.27 cm. Images sampled at ~ 5 Hz.

Velocity and vorticity fields for a static fence and a 1 Hz oscillating fence in a laminar boundary layer are shown in Figure 12 and Figure 13. The yellow line on the images in Figure 12 follows a single vortex structure as it forms, strengthens, and advects downstream. Figure 12 also shows a stable horseshoe-vortex in front of the fence similar to that observed in

the flow visualization studies. From visual inspection, the wake-vortex natural shedding frequency is less than 1 Hz, resulting in a Strouhal number (St) of approximately 0.22. These initial results are consistent with the prior flow visualization studies.

Figure 13 shows one complete fence cycle at the same Reynolds number and a maximum fence height equal to that of the static fence in Figure 12. In the first image the fence is level with the plate surface, and the previously formed vortex advects downstream. The second image shows the fence at approximately half of the maximum amplitude. At this fence height a new vortex is forming. The third image shows the approximate maximum fence amplitude (1.27 cm), where the vortex is at maximum strength. As the fence returns to the plate surface, the vortex separates from the fence and advects downstream in the final two images. Thus, there is one vortex shed per fence oscillation implying that the flow is in the critical flow regime $\phi \sim O(1)$. This is supported by the approximation of ϕ from the estimated natural shedding from Figure 12.

Although clarifying the results from the flow visualization studies is a priority for the PIV measurements, the primary purpose of these initial measurements is to determine the scope of future tests. The traditional method for acquiring PIV images for a flow situation of this type is to phase lock the triggering of the PIV camera with different fence heights. Due to the low fence oscillation frequencies, length of the tow tank, and tow tank settling time, this approach could result in extensive acquisition time to acquire adequate statistical sample sizes at each fence height. This acquisition time will limit the number of flow and test parameters that can be examined.

To decrease acquisition time Proper Orthogonal Decomposition (POD) is currently being examined to reproduce the two-dimensional time-dependent flow fields for the static and 1 Hz oscillating fence flow situations (Durgesh, 2006). If the POD reconstruction adequately describes the flow field, each test run can be sampled at the maximum frequency of the PIV system, providing the maximum number of samples acquired per test run. If the POD approach proves valid, the acquisition time will be reduced and the number of phases will be increased, allowing a more in-depth analysis of the effects and interaction of flow and plate parameters, such as Reynolds number, fence height, fence oscillation frequency, and fence signal.

Resonant Fence Actuator Disturbance Characterization

The decision to use oscillating fences required that we develop an understanding of these little used sensors. Details may be found in the theses and articles given in the publications section (specifically Johnson 2005, Medina 2006a, and Medina 2006b), but the important results are summarized here.

Other mechanical devices that have been studied are variations on a fence oriented in the cross-stream direction which is periodically moved into and out of the flow. Nelson et al. (2000) demonstrated that substantial local pressure disturbances could be created by an oscillating spoiler. Miao et al. (1991b) were able to demonstrate effectiveness in reducing reattachment length behind a backwards step with an oscillating fence. Other studies (Francis et al. (1979), Miao et al. (1995), Miao et al. (1991a), and Nelson et al. (2000)) examining the flow structures created by mechanical oscillating actuators have demonstrated the evolution of the vortical structures generated for a range of frequencies. These prior studies provide details of the characteristics of the flows generated by mechanical oscillation; however all were conducted in relatively low velocity flows and at low oscillation frequencies. This work also built upon the results of Singh reported in the previous section where distinct flow regimes based on a ratio of the actuation frequency (f) and the natural shedding frequency (f_s) of a static fence was established. The drawback of mechanical devices is typically related to relatively complex mechanisms used to create oscillatory movement and the inability to

operate at high frequencies. The most significant positive attribute of a mechanical device is that it extracts energy from the flow itself and therefore its effectiveness will scale with the flow. This is unlike most other unsteady actuation devices that have authority fixed by characteristics of the device independent of the flow.

Before employing the oscillating fence actuator on an airfoil, it was necessary to design an actuator that could operate with the frequency and amplitude necessary for our application. Furthermore, it was desired to characterize the actuator at Reynolds numbers higher than those of the previous studies that were more applicable to the regime in which we wanted to test. Below the actuator and the disturbances it produces are discussed. Static, transitioning, and oscillating fences were studied and are reported by Medina (2006b), but here the discussion will be limited to the oscillating case.

Actuator Design, Test Facility, and Instrumentation

The actuators used in this study are shown schematically in Figure 14. This mechanical actuator oscillates a 76mm wide fence positioned perpendicularly to the surface of the flat plate. The fence is attached to cantilever springs and is forced by a voice coil and magnet. Extruded carbon fiber rods were used for the cantilever springs. The fence position is monitored through the use of a small laser and silicon light detector placed inline with the bottom edge of the fence. The fence is forced at its natural resonant frequency, thus requiring a low power input. The maximum power consumed by the actuators used in this study was less than 1.5 watts of AC power.

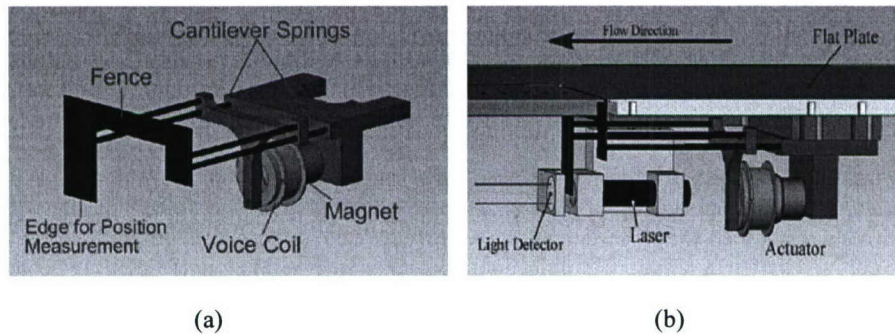


Figure 14- Actuator schematics from two different vantage points showing important components: (a) actuator showing important mechanical/electrical components, and (b) actuator installed in flat plate showing position detection components.

The actuator is mounted on the flat plate such that the top edge of the fence is even with the plate surface in its neutral or "off" position. Consequently the flow experiences half-sine motion from the fence. The fence rises from phase angles $\theta_f = 0$ to 90 , reaches its peak at $\theta_f = 90$, and descends from phase angles $\theta_f = 90$ to 180 . For the remaining portion of the actuator phase, $\theta_f = 180$ to 360 , the actuator motion occurs beneath the plate. Two sets of carbon fiber rods of different diameters were used in the current experiments. The separate sets of rods change the resonant characteristics of the actuators providing for different test frequencies. Actuators made with the smaller diameter rods were capable of producing 10mm fence heights at 50-60 Hz resonant frequencies. The range of frequencies was due to differences in individual actuators with the same rod diameters. Changes in fence mass and inherent variations in the springs produced small changes in the individual resonance of the actuators. The resonant bandwidth of a specific actuator was ~ 0.2 Hz. Actuators made with the larger diameter springs were capable of 6 mm fence heights at 105-112 Hz resonant frequencies. A systematic optimization of actuator geometries or materials was not performed; consequently, there may be significant opportunity for increased actuator performance.

Experiments presented in this paper were conducted on a flat plate in a low-speed, open-loop wind tunnel with a 0.30m x 0.30m cross-section and 2.4m test section at the University of Wyoming. The ceiling of test section consists of six moveable plates that can be adjusted to produce varying pressure gradients along the length of the test plate. The flat plate positioned to produce a zero pressure gradient boundary layer for this study. The flat plate shown in Figure 15 is a 6.4 mm thick, one meter long plate located 0.30 m downstream from the start of the test section. The plate is mounted to the wind tunnel floor using a 65 mm riser faring that also serves to conceal the actuator and pressure sensing equipment. The wind tunnel sidewalls and ceiling are made from clear Lexan providing for optical access from the sides and top.

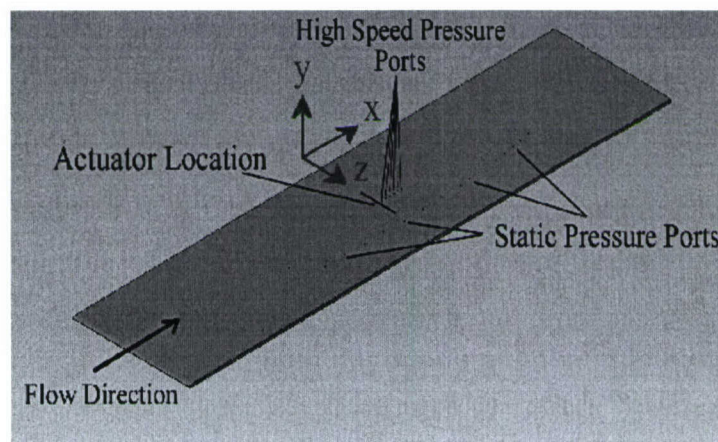


Figure 15 – Flat plate schematic showing actuator location and associated coordinate system.

The measured free-stream turbulence intensity above the plate is 0.26 percent. The transition to a turbulent boundary layer is triggered by a small separation at the leading edge of the plate. This small separation functions as a trip for the boundary layer which accelerates its development. The actuator is located at 0.648m from the leading edge. Flow two-dimensionality and boundary layer characteristics have been determined at the actuator location through hot wire surveys. A three-axis traverse was used for precise position control of hot wire surveys. Movement resolution was 0.025 mm. Fifteen static pressure ports are located along the length of the plate for the purpose of setting the pressure gradient along the plate and calibration of high speed pressure transducers.

Several different diagnostics were used in this study for various purposes. High speed pressure transducers were used to characterize the pressure footprints behind the actuators. PIV was used to reveal the two-dimensional flow field behind the fence. This revealed the formation and dissipation of large coherent structure generated by the fence. Hot wire anemometry was used to characterize the turbulent boundary layer and measure energy spectra at different positions in the flow. A brief description of each of these instruments is provided below.

High speed dynamic pressure transducers were positioned at six locations downstream of the actuator location along the actuator center line. These locations (10.2mm, 20.3mm, 30.5, 40.6, 50.8, and 61.0mm) are indicated in the PIV Figures by vertical black lines. Dynamic pressures were measured with piezo-resistive pressure transducers mounted flush with the top surface of the plate. The sensor non-repeatability level is less than 1 percent of the lowest pressure levels measured in this test. The sensors were calibrated in-situ prior to individual test runs. Calibration was performed by fitting sensor output voltages to static pressure measurements appropriate for the sensor locations over a range of wind tunnel velocities. These sensors were used to make repeated measurements for transitioning fence tests and phase-averaged

measurements for oscillating fence tests. The reported transition pressures are the ensemble average of 500 pressure measurements. Oscillating fence pressures are the result of 100 to 300 phase-averaged cycles. The pressures can be decomposed into mean pressures and fluctuating pressures that are comprised of turbulent fluctuations, and actuator induced fluctuations.

Particle Image Velocimetry was employed for velocity measurements in the x - y plane (see Figure 15 for the plane directions). The flow was seeded with atomized oil and was illuminated with twin 50mJ Nd:YAG lasers. Image pairs were captured using a 1392 x 1024 pixel camera. Velocities were calculated via cross-correlation using a multi-pass decreasing window size technique. Phase-locked measurements were taken at specific points within the actuator cycle to resolve the phase-averaged velocity field generated by the actuator. The PIV laser head was mounted from the top of the test section to provide a light-sheet which illuminated an x - y cross section of the actuator and the flow field downstream of it. The PIV camera was placed along side of the test section at the actuator location and perpendicular to the light sheet. The typical image area for this test was 70mm x 50mm. Each PIV single phase result was produced from 100 phase-locked measurements. The PIV images contained in the paper are velocity vectors plotted over vorticity contour levels.

Constant temperature hot wire anemometry was used to characterize the flat plate boundary layer and to measure energy spectra at various locations within the flow. The hot wire used was a 2.5 μ m diameter tungsten wire. Calibration was performed by using a King's Law fit to Pitot-static tube velocity measurements prior to each test. The hot wire was located at the end of a boom that was inserted into the wind tunnel from behind the flat plate and attached to the three-axis traverse. Boundary layer velocity profiles were taken at locations across and upstream of the actuator position. These profiles were used to determine characteristic boundary layer values.

Boundary Layer Characterization

The turbulent boundary layer just upstream of the sensor was characterized for the different test conditions using boundary layer surveys such as that shown in Figure 16. For reference, the different fence heights tested are shown and indicate that the fence heights are a substantial fraction of the boundary layer thickness. The boundary layer conditions for the cases tested are summarized in Table 2.

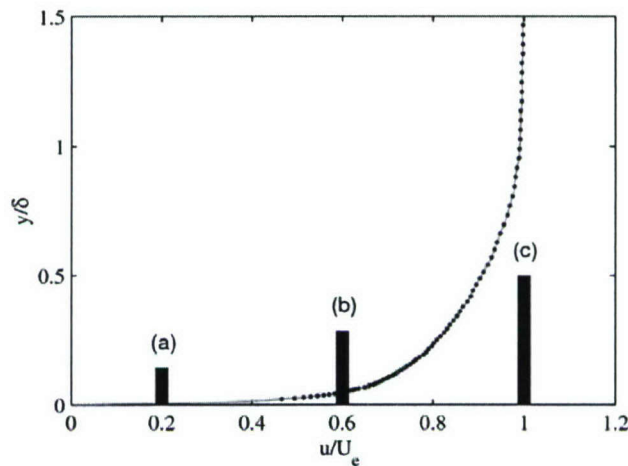


Figure 16 – Boundary Layer Survey with curve fit and tested fence heights superimposed.

Table 2 – Boundary layer parameters for the cases tested. U_e is the edge velocity, δ_{99} is the 99% boundary layer thickness, δ^* is the displacement thickness, θ is the momentum thickness, Re_x is the Reynolds number based on distance from the leading edge, Re_θ is the Reynolds number based on momentum thickness, and H is the shape factor.

U_e	δ_{99}	δ^*	θ	Re_x	Re_θ	H
20.0m/s	0.0217m	0.0034m	0.0025m	$6.90 \cdot 10^5$	2664	1.36
18.4m/s	0.0201m	0.0034m	0.0025m	$6.36 \cdot 10^5$	2456	1.36
16.0m/s	0.0202m	0.0035m	0.0025m	$5.53 \cdot 10^5$	2135	1.40
13.5m/s	0.0211m	0.0036m	0.0026m	$4.66 \cdot 10^5$	1872	1.38
11.2m/s	0.0210m	0.0039m	0.0027m	$3.85 \cdot 10^5$	1605	1.40

Resonant Fence Actuator Characterization

This study considered fifteen different oscillating fence cases representing a range of Reynolds number, Strouhal number and fence height to boundary layer thickness. High speed pressure measurements and phase-locked PIV measurements were made for each of these cases. For detailed results see Medina 2006a and 2006b, but an overview will be provided here.

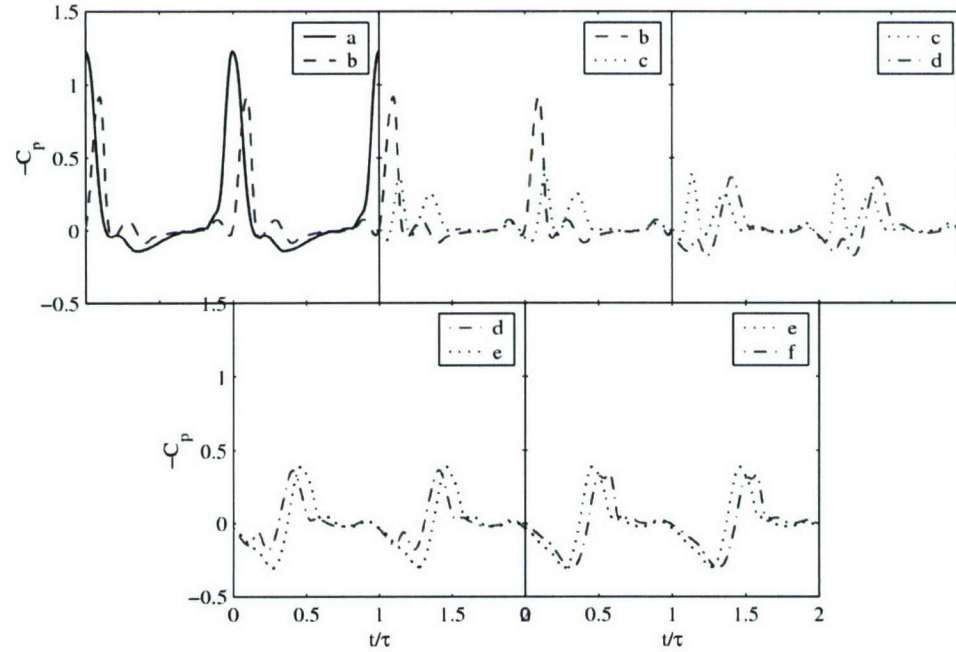


Figure 17 – Pressure footprint for $Re_h = U_h h / \nu = 7109$, $h/\delta = 0.476$, and $St_a = f h / U_h = 0.036$: (a) $x/h = 1.02$, (b) $x/h = 2.03$, (c) $x/h = 3.05$, (d) $x/h = 4.06$, (e) $x/h = 5.08$, and (f) $x/h = 6.10$.

A typical pressure footprint for one of the cases (case 10 in 2006a) is shown in Figure 17. Each of the six pressure transducer results represents a phase averaged values. Phase-averaged PIV results at different points in the actuator cycle for the same case are shown in Figure 18.

Several important items should be noted about these results. First, a very strong pressure suction peak is created at the first two downstream locations (a and b in Figure 17). At these locations, the vortex is located close to the surface and is well-organized as is evident in Figure 18(a)-(c). As the vortex convects downstream, it exhibits upward movement that

results in a sharp decrease in peak suction between pressure taps at locations b and c. As the primary suction peak decays, a secondary suction peak develops and strengthens with downstream distance and has an equally strong pressure peak (negative suction) that precedes it (in time). This pattern that is seen for position d-f suggests the presence of a secondary vortex that is induced by the first vortex as it moves away from the plate.

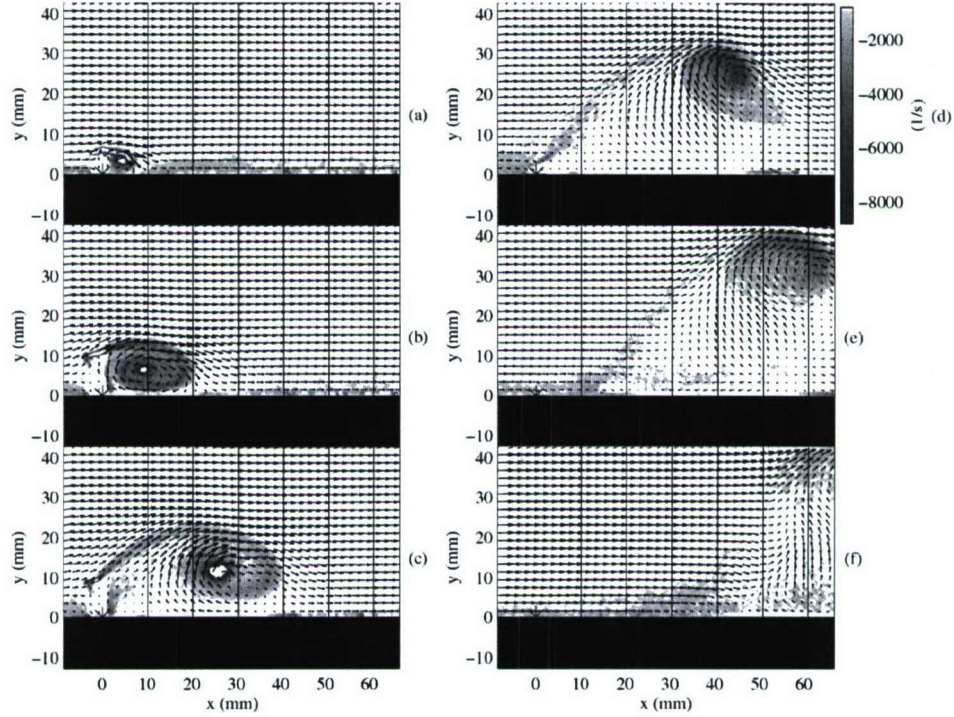


Figure 18 – PIV vortex development at different phases θ_f in the oscillation cycle for $Re_h = U_h h / \nu = 7109$, $h/\delta = 0.476$, and $St_a = fh/U_h = 0.036$: (a) $\theta_f = 45$, (b) $\theta_f = 90$, (c) $\theta_f = 135$, (d) $\theta_f = 180$, (e) $\theta_f = 225$, and (f) $\theta_f = 270$. The fence location is denoted by a *, and the locations of the six pressure transducers are indicated by the vertical lines.

Similar results were obtained from the other test cases studied. From these results, conclusions about the effects of fence height (h/δ) and fence frequency ($St_a = fh/U_h$) could be determined. For a fixed frequency f , smaller h/δ values resulted in the generation of weaker vortices that rapidly dissipate. Larger h/δ values produced stronger vortices, but they tended to lift off the surface. This suggests that, from a pressure footprint point of view, there may be an optimum value of h/δ that produces a vortex of a strength significant enough to produce a reasonable pressure change, but not so large to cause it to lift off the surface. At locations nearest to the fence, the largest suction peaks were always associated with the largest fences.

The actuator frequency also appears to have effects on the vortices generated and the resulting pressure footprints. Slower actuation frequencies tend to produce weaker, stretched-out vortices compared to higher actuation frequencies when the fence height is held constant. Consistent with this observation was the higher suction peaks observed for the higher frequency actuation. However, the effect on suction peak is much smaller than that produced by changing fence height.

A discussion of other observations, such as the appearance of a third pressure peak for low St_a and high fence height, are presented in Medina 2006a.

Of greatest importance for load controlling applications is how much of a disturbance can be produced and what is its effect on local lift. The pressure integrated over a single cycle at each pressure location downstream of the fence. As can be seen, the contribution upstream of 40 mm downstream is generally positive, whereas the pressure downstream of 40 mm is generally negative. Obviously the picture is incomplete since we would have to go further downstream to fully characterize this picture. The integral under the complete curve would represent the net lift increase (or decrease) produced by this actuator. One interesting case is the curve labeled test case 15. This case has a large St_a and large h/δ relative to the other cases. This case does not have a large pressure peak to go along with its suction peak, which explains why it retains its positive lift value. More work is needed to explore this type of case.

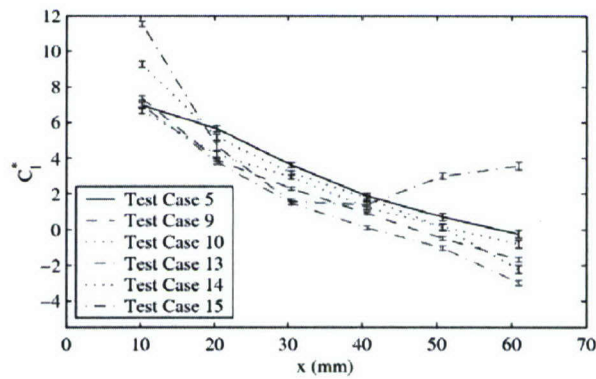


Figure 19 – Lift contributions from six pressure measurement positions

In summary, a range of actuator heights and Strouhal numbers have been tested. The actuators appear to produce a significant disturbance that could be used to produce net lift if the actuator parameters are chosen carefully. Further details of quantifying the disturbances produced are given in Medina 2006a. One final question that should be considered is how such a disturbance might be used in a load control application.

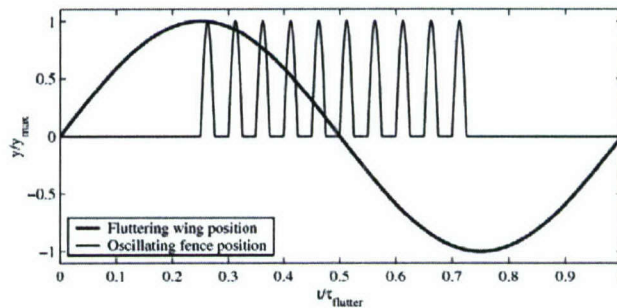


Figure 20 – Actuator operation for a fluttering wing.

The pressure signals from the sensors indicate that a positive lift contribution is obtained with each oscillation of the fence. For periodic control applications such as a fluttering wing, lift augmentation would only be desirable over the downward movement of the wing, as demonstrated in Figure 20. The actuator is made active during downward motion of the wing.

The resulting lift contribution from the actuator would act in opposition to the movement of the wing resulting in a dampening of the flutter motion.

The on/off operation of the actuator could be accomplished through amplitude modulation or frequency modulation. Amplitude modulation is accomplished by simply modulating the amplitude of the sinusoidal voltage being applied to the actuator, and thus changing the resultant fence height. Frequency modulation is accomplished by taking advantage of the resonant characteristics of the actuator. Since the usable resonant bandwidth of the actuator is narrow (~ 1.5 Hz), small changes to the forcing frequency (~ 1 Hz) result in near complete reduction in the oscillation amplitude. Thus, fence height modulation can be performed with small variations to the forcing frequency.

Although these results are promising, the real question is can they be employed to modify lift on an actual airfoil? To answer this question, actuators must be tested on an airfoil which is the focus of the next section.

Resonant Fence Actuator Used on an Airfoil

In order to use flow control for fluttering airfoils, a disturbance of strength sufficient to produce a significant change in the loads on the wing must be achieved. The fence actuator concept has shown promise in a flat plate turbulent boundary layer, but it ultimately must be tested on an oscillating airfoil to verify the disturbance strength. This section discusses an experimental effort focused on characterizing disturbances in an airfoil flow.

Experimental Setup

All the experiments presented in this section were conducted in the University of Wyoming Aeronautical Labs 0.61 m x 0.61 m wind tunnel that has a 1.22 m long test section. This wind tunnel is capable of producing free-stream velocities of up to 50 m/s with a free-stream turbulence intensity of 0.7% of the free stream velocity. The Reynolds number based on chord (Re_c) used for this study ranged from 2.5×10^5 to 7.5×10^5 .

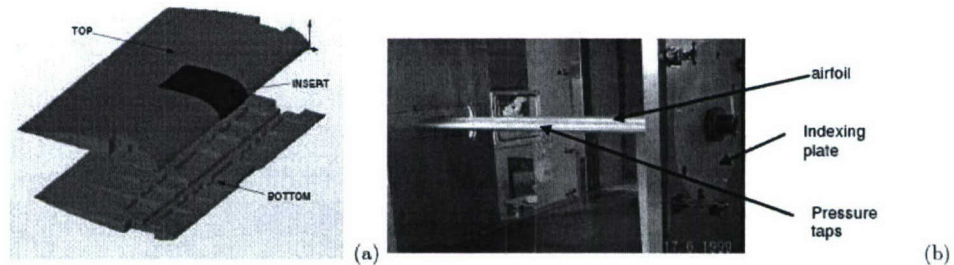


Figure 21 – NACA 2301 airfoil used in the present study: (a) airfoil assembly, and (b) airfoil installed in the wind tunnel.

The Airfoil

A NACA-23012 airfoil with a 24-inch span and 12-inch chord was manufactured in three parts (top, bottom, and insert) and is shown in Figure 21(a). The airfoil is designed with pockets to enclose the pressure transducers. Different inserts can be machined to suit the instrumentation needs of an experiment, thus making this design very versatile. The top (including insert) and bottom surfaces of the airfoil each have ten mounting locations for high speed pressure transducers and 32 static pressure ports. For the static fence experiments, a slotted insert was made and the fence itself is made from 1.27 mm thick and 101 mm wide shim stock. Initial measurements showed that the boundary layer was laminar. A simple

window mesh was used at the leading edge to trip the boundary layer. The airfoil is shown installed in the wind tunnel in Figure 21(b).

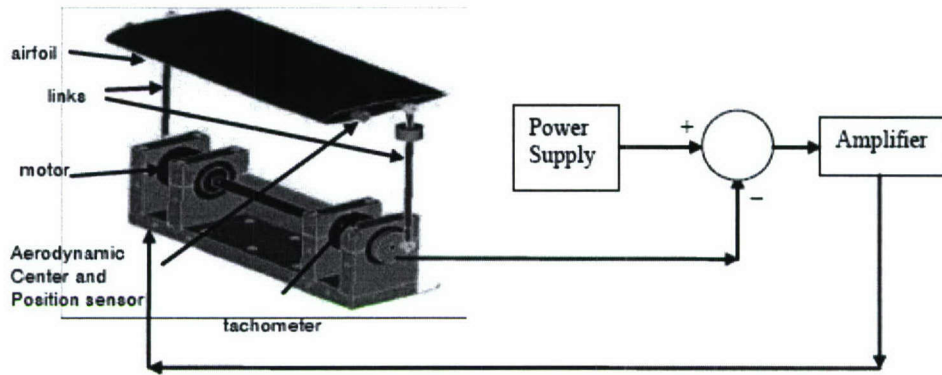


Figure 22 - Schematic of oscillating airfoil and its control electronics.

Instrumentation and Data Acquisition

With the current setup, the airfoil can be oscillated about the quarter-chord point using a feedback circuit, the schematic for which is shown in Figure 22. The instantaneous angle of attack of the airfoil in dynamic motion, is defined as $\alpha_i = \alpha_m + \alpha_o \sin(2\pi f_f t)$, where t is the time. For this setup, the mean angle of oscillation (α_m) can be varied from -5° to 5° . Oscillation amplitude (α_o) and maximum oscillation frequency (f_f) are fixed at $\pm 5^\circ$ and 4 Hz, respectively. The instantaneous position of the airfoil is determined using a RVIT-15-60 rotary transducer. A mixture of Kulite model XCS-093-2D and Entran model EPE-541-2P pressure transducers was used to measure the instantaneous surface pressure on the airfoil. Validyne model SG297A modules act as power supply and signal conditioners for the pressure transducers. The pressure signals are then low pass filtered at 3000 Hz and connected to a high speed simultaneous sampling (NI-6123) data acquisition system. One hundred independent records are acquired for each case at 6250 Hz for 2 seconds.

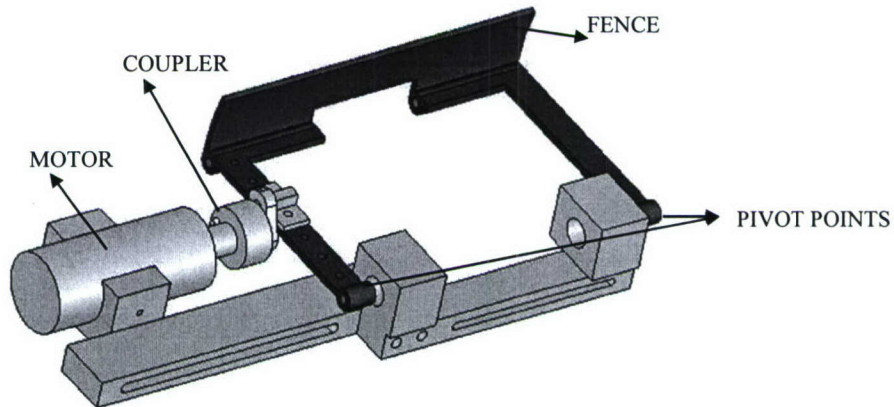


Figure 23 - Schematic for Oscillating Fence Actuator.

Oscillating Fence

The schematic of the actuator is shown in Figure 23. A DC motor with a digital encoder is used to determine and also to control (using a software PID controller) the instantaneous frequency of the fence. Although not shown in this figure, a potentiometer is installed on one of the pivot points to provide the instantaneous position of the fence. Currently, the maximum frequency that can be attained with this device is 40 Hz. The major advantage of this design is that it allows the user to select the operating frequency (f_a) and height (H) and therefore, allows one to span a number of experimental variables like Strouhal Number and H/δ .

Results

All of the baseline/preliminary testing has been finished. These tests can be categorized into five categories: characterization of the boundary layer on the airfoil, characterization of stationary airfoil, characterization of oscillating airfoil, flow over stationary airfoil with static fence, and flow over oscillating airfoil with static fence. Each of these is discussed below. For additional detail, see Saini et al. (2006). At the end of this section, the testing currently being undertaken is briefly described.

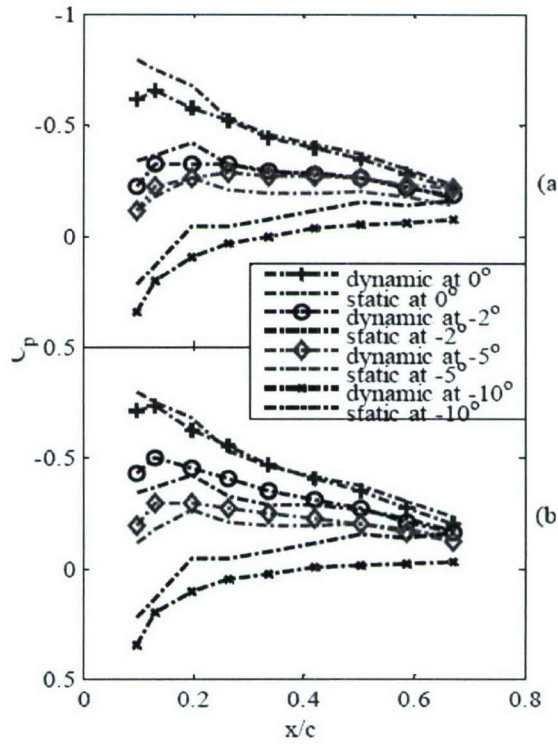


Figure 24 - Pressure Distribution on oscillating airfoil for a mean angle -5° and $U_\infty = 35$ m/s for a) up-cycle, and b) down-cycle.

Turbulent Boundary Layer Characterization

As a first step, Oil Film Interferometry (OFI) was used to determine the nature of the flow. The results showed that the flow was laminar over the airfoil with a skin-friction coefficient (C_f) equal to 1.3×10^{-3} at $x/c = 30\%$. A simple window mesh was therefore used to trip the boundary layer. This resulted in a turbulent boundary layer and C_f at the same location (30% x/c) had increased to 5×10^{-3} . Hotwire measurements were then performed at 0° angle of attack to determine the boundary layer thickness as a function of chord-wise distance from the

leading edge. It was seen that, within the insert region, the boundary layer thickness is quite small and varied approximately from 2mm to 4mm. There also appeared to be little effect of velocity on the boundary layer thickness.

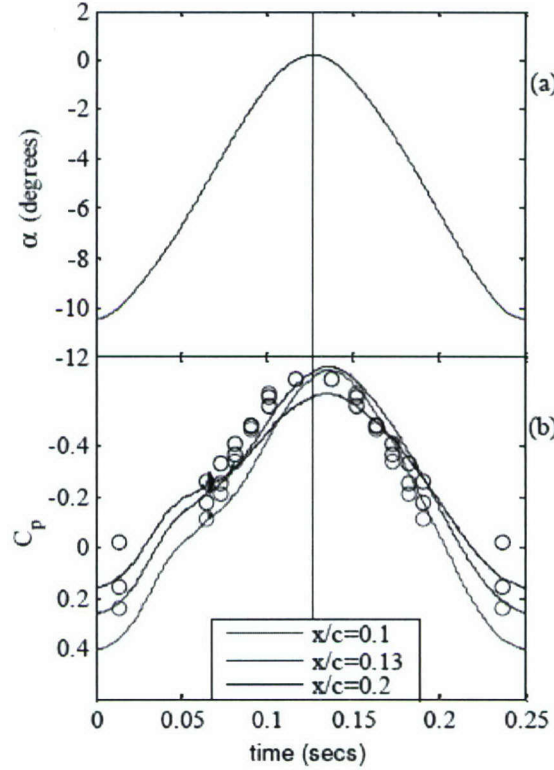


Figure 25 - Time history of a) position and b) pressure distribution for $\alpha_m = -5^\circ$ and $U_\infty = 35\text{m/s}$. Solid lines are for oscillating airfoils, whereas circles are the results for the stationary airfoil.

Characterization of the Stationary airfoil

To ensure that the airfoil was producing a flow that had the desired characteristics, pressure readings were acquired and compared against results from inviscid flow theory. The comparison showed a fairly good agreement. As a result, the oscillating airfoil was next considered.

Characterization of the Oscillating Airfoil

Three different free-stream velocities (U_∞) of 25 m/s, 35 m/s, and 45 m/s were used to confirm the independence of C_p with respect to U_∞ . Results for mean angle (α_m) of -5° are shown in Figure 24. The up-cycle refers to the portion of oscillation cycle during which the angle of attack is increasing, and the down-cycle refers to the portion with a decreasing angle of attack. For the most part, the results are intuitive, and the pressure lags for the up-cycle and leads for the down-cycle compared to the pressure distribution for stationary airfoil at the same angle of attack. It was also observed that, as expected, the flow remains attached beyond the static stall angle. This effect has been seen in past studies done on pitching-up airfoils.

However, some cases show a deviation from the expected results. For example, in Figure 24(a) during the up-cycle, the pressure distribution for -5° degrees lags the stationary airfoil pressures, the -10° leads the stationary airfoil pressures during the down-cycle in Figure 24(b).

It was also observed that, for the down-cycle, the pressure distribution for 5° lags the stationary airfoil pressures. To investigate this unexpected behavior, phase-averaged time histories were studied. The position and pressure as a function of time at mean angles of -5° are shown in Figure 25. Corresponding values of C_p for stationary airfoil at corresponding angle of attack are plotted as symbols. It is seen that the C_p curves are asymmetrical about the peak. Also, it can be observed that the pressure distribution on the oscillating airfoil responds slowly during the up-cycle and faster during the down-cycle. At the beginning of up-cycle, the pressure distribution lags the stationary airfoil pressure distribution significantly. At around -5° , the pressures for the stationary and oscillating airfoil are in phase. The oscillating airfoil pressure distribution lags again as the airfoil approaches the peak angle of attack. During the down-cycle, the oscillating airfoil pressure distribution is almost in phase with stationary airfoil pressure distribution except at the end of cycle where a significant lag is observed. For the mean angle of 5° , it was observed that the airfoil seems to be responding slowly during the down cycle and faster during the up-cycle and that the pressure distribution for the oscillating airfoil lags the stationary airfoil pressure distribution for the up-cycle and leads for the down-cycle. To further investigate this behavior, PIV measurements were conducted using 10 phase locked position for a given mean angle over 1 complete cycle. 100 images were averaged over each of these locations. However, these measurements did not show existence of any structure that would further explain the asymmetric pressure distribution.

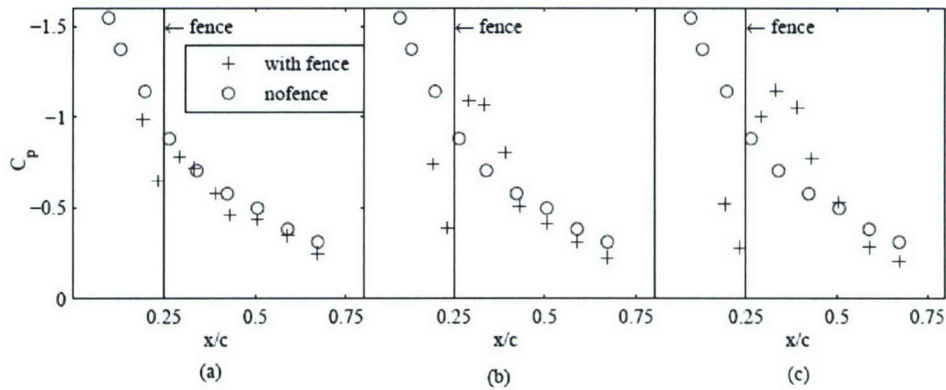


Figure 26 - Pressure distribution on stationary airfoil without and with a) 1 mm, b) 3mm, and c) 5 mm fences at $\alpha=0^\circ$ and $U_\infty = 35$ m/s.

Stationary Airfoil with Static Fence

Three different fence heights (1 mm, 3 mm, and 5 mm) were selected based on results obtained from hot wire anemometry results discussed before. All three heights were tested at three different locations, namely, $x/c = 15\%$, 25% , and 35% .

Figure 26 shows the results for three fence heights at $x/c=25\%$ as compared to a stationary airfoil at same angle of attack but without fence. As can be seen, the presence of the fence causes a suction peak and a pressure peak aft and ahead of the fence and as we move away from the fence the pressure distribution approaches the no fence case. As the fence height is increased this effect becomes prominent. This effect is similar to the pressure distribution caused by the deployment of a spoiler to dump lift in an aircraft. Although not shown here, the effect of changing the fence location is just to move the suction and pressure peak to the fence position.

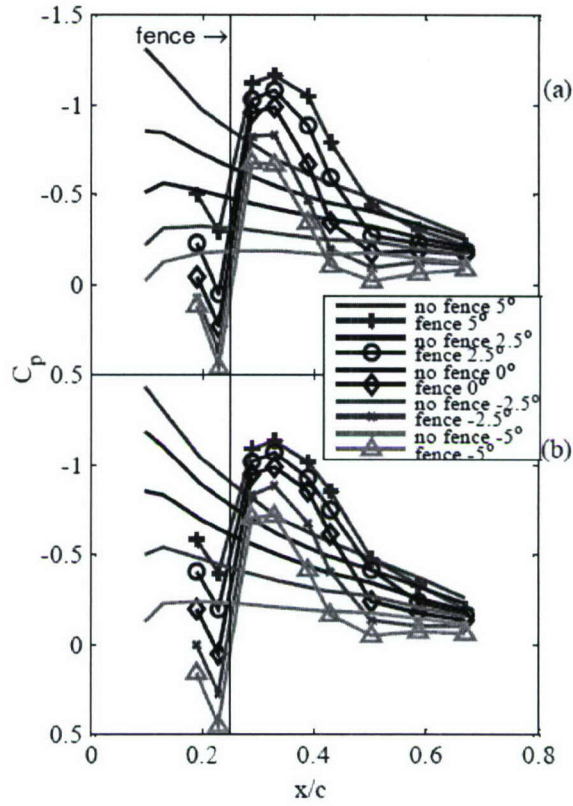


Figure 27 – Pressure distribution on airfoil oscillating about 0° , without and with a 5mm fence for a) up-cycle, b) down-cycle.

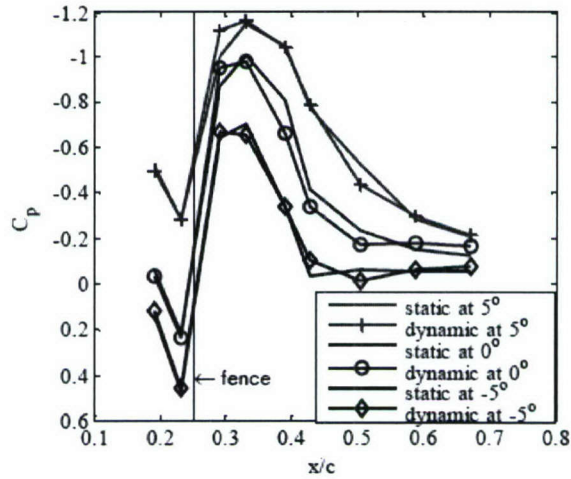


Figure 28 - Pressure distribution on oscillating and stationary airfoil with 5mm static fence.

The objective of studying a stationary fence on an oscillating airfoil was to identify the effects of the fence compared to those found in the baseline oscillating airfoil case. Figure 28 compares the pressure distribution on an airfoil oscillating, with and without a fence, about mean angle of 0° . The cases shown are for $U_\infty = 35$ m/s and fence height of 5mm. As was

noted in the previous section, the suction peak right behind the fence and a pressure rise just before the fence are clearly evident from the plots.

As the downstream distance increases, the difference between the fence and no fence cases becomes small and the effects are more pronounced for the up-cycle than for down-cycle. Qualitatively the same behavior was seen for fence heights of 1mm and 3mm. To compare the effect of a static fence on an oscillating and stationary airfoil, Figure 28 is shown during the up-cycle. The mean angle for the oscillating case is 0° , and the fence height is 5 mm. No appreciable difference can be noted for the oscillating and stationary airfoil. Other cases also did not show any substantial differences. This is an important finding because this shows that the authority of the fence to produce disturbances is unaffected by the oscillations of the airfoil.

Ongoing Work

As was discussed earlier, unexpected asymmetrical pressure distributions over the baseline oscillating airfoil (no fence) were observed. Also, further attempts, using PIV, to explain this behavior were not successful. Numerical simulations are being conducted to find a possible explanation for this observed phenomenon.

On the experimental side, tests are currently being conducted on stationary airfoil with oscillating fence. The fence position is fixed at $x/c = 35\%$. Angles of attack are the same as those for the baseline stationary airfoil case. Along with the surface pressure measurements, simultaneous PIV readings are also being conducted. These tests will help in characterizing the performance of the actuator at different angles of attack.

Once the stationary airfoil cases are finished, tests will be conducted on oscillating airfoil with oscillating fence configuration to access the authority of the fence to counter the oscillating motion. A major challenge here appears to be implementation of double phase locking (i.e. the phase of airfoil and fence oscillation) to generate a trigger. Bench top testing revealed that simultaneous occurrence of two events is rare and can add large uncertainties to the measurements. To avoid double phase locking, use of proper orthogonal decomposition (POD), implemented using PIV triggered at random fence locations, is being explored. A velocity field obtained using PIV for stationary airfoil at 0 degrees and random fence location is shown in Figure 29. If successful, this approach will require phase locking on the airfoil phase only.

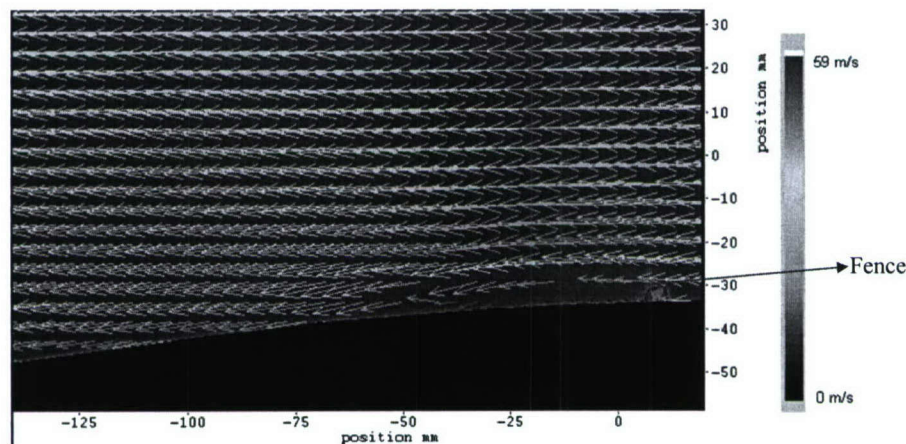


Figure 29 - Caption Velocity field obtained using PIV on stationary airfoil with oscillating fence at $\alpha=0^\circ$ and random fence height.

Control Issues for Fluttering Wing

Closed Loop Control

The closed loop control problem is to design a controller that utilizes a cooperative set of actuators to create beneficial lift and moment in order to dampen out the oscillatory flutter modes of a given system. The system that is used here is a 2-D typical section shown in Figure 30. It can be thought of as 3-dimensional half wing mounted as a cantilever beam to the side wall of a wind tunnel. The vertically mounted spring gives the system a plunge mode and the torsional spring at point E gives the system torsional modes. The system also has two unsteady, internal, aerodynamic feedback modes.

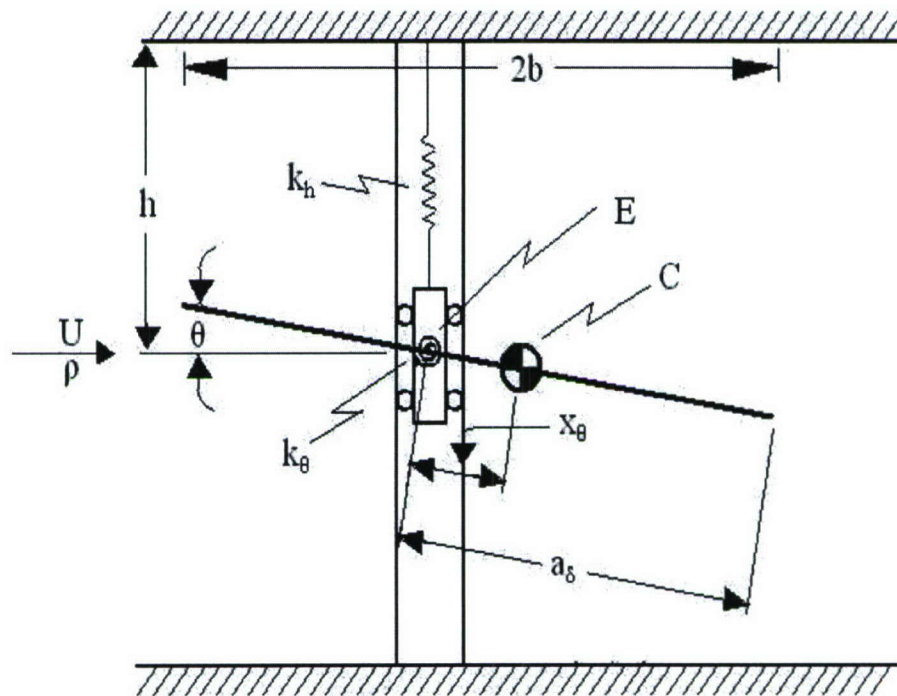


Figure 30 – Fluttering airfoil system used for control.

The equations of motion for this system are:

$$\begin{aligned} 0 &= m(\ddot{h} + x_\theta \ddot{\theta}) + L + k_h h \\ 0 &= \bar{J}_\theta \ddot{\theta} + x_\theta m(\ddot{h} + x_\theta \ddot{\theta}) - M + k_\theta \theta \end{aligned}$$

Through observation in the wind tunnel; the actuators have been shown to create a pressure foot print on a flat plate similar to the curve in Figure 31, and can be approximated by the equation

$$C_{p_u} = -\frac{1}{16\sqrt{2\pi}} e^{\frac{-x^2}{512}} U_u$$

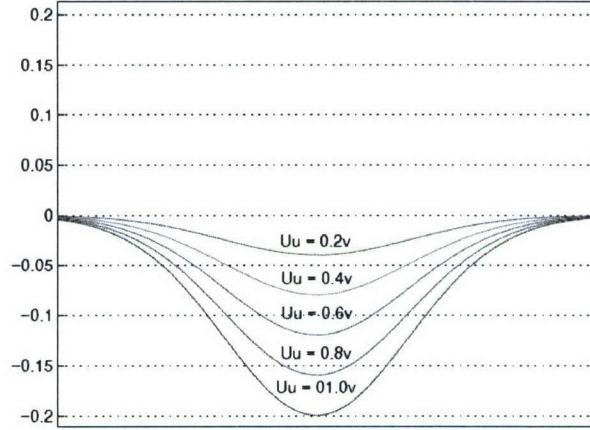


Figure 31 – Model disturbance used for control development.

The system can be written as:

$$\dot{x} = Ax + Bu_a \quad \ni$$

$$A = \begin{bmatrix} 0 & 0 & 1 & 0 & 0 & 0 \\ 0 & 0 & 0 & 1 & 0 & 0 \\ -M \setminus B + \frac{1}{2} \eta M \setminus RU^2 S_1 & -M \setminus K + \frac{1}{2} \eta M \setminus RU S_2 & \frac{1}{2} \eta M \setminus R & & & \\ AKU^2 S_1 & AKU S_2 & -0.0455 & 0.0 & & \\ BKU^2 S_1 & BKU S_2 & 0.0 & -0.30 & & \end{bmatrix} \quad x = \begin{bmatrix} h \\ \theta \\ \dot{h} \\ \dot{\theta} \\ x_{a1} \\ x_{a2} \end{bmatrix} \quad B = \begin{bmatrix} 0 \\ 0 \\ \frac{\ell_a}{m} \\ \frac{m_a}{m x_g^2} \\ 0 \\ 0 \end{bmatrix}$$

For the LWR control design, we will assume that the matrix $D=0$, and the matrix C is a mapping such that $y = [h \quad \theta]^T$. Assuming all states are observable, we found a vector $k \ni$

$$u = -kx$$

that minimizes the cost functional

$$J = \int (x^T Q x + u_a^T R u_a + 2 * x^T N u_a) dt$$

subject to

$$x(0) = [1 \quad 0 \quad 0 \quad 0 \quad 0 \quad 0]^T$$

and $x(\infty)=0$. For these simulations, Q , R , and N were defined as

$$Q = \begin{bmatrix} 100 & 0 & 0 & 0 & 0 & 0 \\ 0 & 100 & 0 & 0 & 0 & 0 \\ 0 & 0 & 100 & 0 & 0 & 0 \\ 0 & 0 & 0 & 100 & 0 & 0 \\ 0 & 0 & 0 & 0 & 1 & 0 \\ 0 & 0 & 0 & 0 & 0 & 0 \end{bmatrix}, N = \begin{bmatrix} 1 \\ 1 \\ 1 \\ 1 \\ 1 \\ 1 \end{bmatrix}, R = 10.$$

As you can see from Figure 32 below, the LQR controller reduced the settling time of the system by a factor of 10. Also, analyzing the plots below, the LQR controller increased the airspeed which causes onset of flutter by 20 %. Let the normalized airspeed be:

$$\bar{U} = 0.8 \frac{U}{b\omega_h}$$

Comparing Figures 33 and 34, it can be seen that the plunge modes are the source of flutter instability because these modes cross over the real axis (thus becoming unstable) at lower airspeed than the aerodynamic modes. While the flutter phenomena still occurs in the closed loop system, it happens at higher airspeed ($\bar{U}=6.8$).

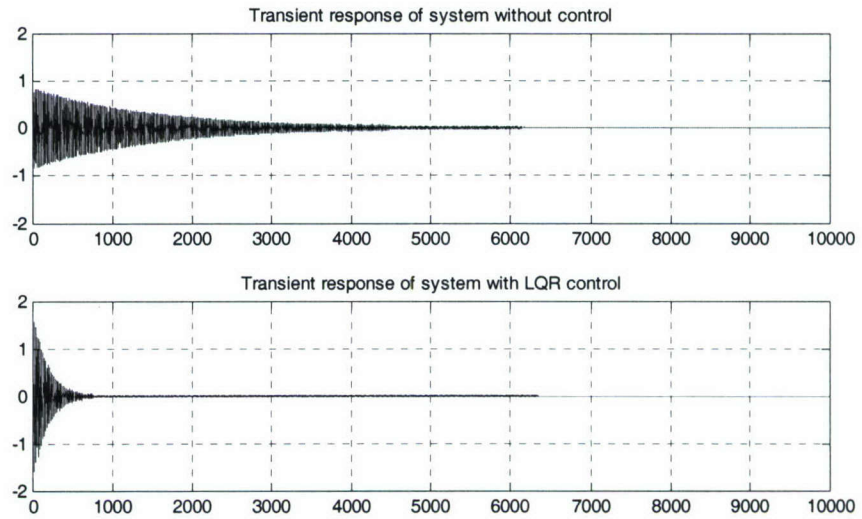


Figure 32: Transient Time responses of the system without and with the control algorithm.

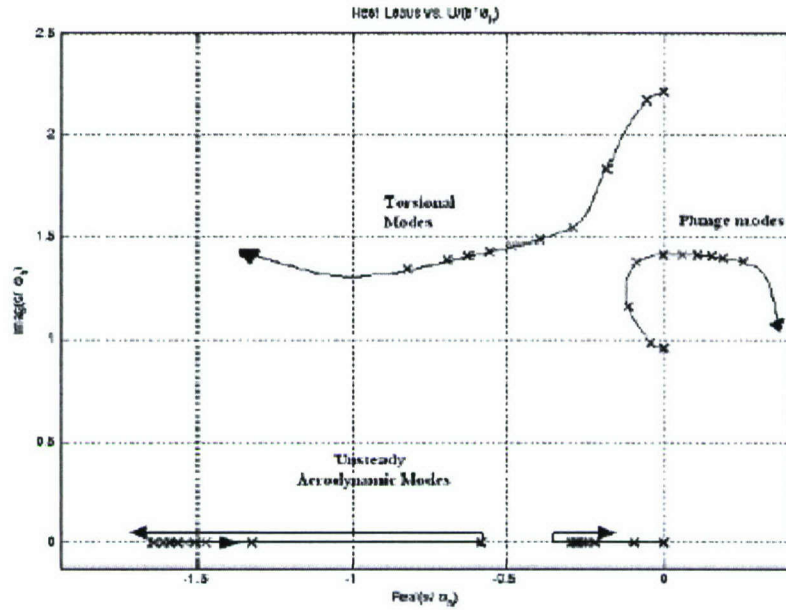


Figure 33: Root Locus of Typical Section as U bar varies from 0 to 7.2

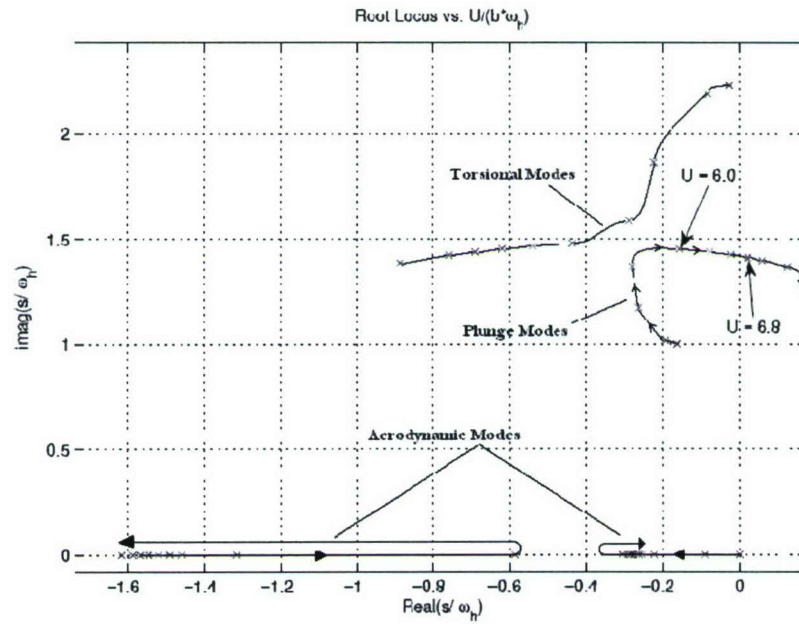


Figure 34: Root Locus of Controlled System as U bar is varied.

Conclusions and Future Work

In this study, the use of actuators that use the flow's energy to produce disturbances suitable for controlling flutter has been investigated. Laminar flat plate flow studies, turbulent flat

plate flow studies, turbulent flow over wings and the use of actuators in actual control have all been investigated. As is evident from the work presented here, we have made good progress toward creating and characterizing disturbances created by oscillating fence actuators that promise to be of sufficient strength for use in flutter control. In addition, we have considered how such disturbances might be used to control flutter. However, the use of localized aerodynamic control for this problem is still immature, and further work is necessary before the full potential of this approach is realized. However, the payoff of such a system will be large since there are many platforms that could benefit from the lightweight, low power flutter control system that this approach could yield.

The next steps in the research here would be to apply the actuators to control a real model. For instance, a simple pitching model or a pitch/plunge model using a two-dimensional airfoil could be used to conclusively demonstrate that, not only can we create disturbances of sufficient strength to control flutter, but that they can be used in such a manner to effectively control flutter.

References

- Bushnell, D. M., and McGinley, C. B., 1989, "Turbulence Control in Wall Flows," *Annual Review of Fluid Mechanics*, 21, 1-20.
- Durgesh, V., Naughton, J.W., 2006, "Detailed Experimental Investigation of the Base Drag Reduction Phenomena on a Wedge Model," *AIAA Paper 2006-3186*, 3rd AIAA Flow Control Conference, San Francisco, CA, June 5-8.
- Fiedler, H. E., and Fernholz, H.-H., 1990, "On Management and Control of Turbulent Shear Flows," *Progress in Aerospace Science*, 27, pp. 305-387.
- Francis, M. S., Keesee, K. E., Lang, J. D., Sparks, G. W. Jr., and Sisson, G. E., "Aerodynamic Characteristics of an Unsteady Separated Flow. *AIAA Journal*, 17(12):1332--1339, December 1979.
- Giurgiutiu, V., Chaudhry, Z., and Rogers, C. A., 1995, "Effective Use of Induced Strain Actuators in Aeroelastic Vibration Control", in *Proceedings of the 36th AIAA/ASME/ASCE/AHS/ASC Structures, Structural Dynamics, and Materials Conference and Adaptive Structures Forum*, New Orleans, April 13-14.
- Greenblatt, D., and Wagnanski, I.J., 2000, "The Control of Flow Separation by Periodic Excitation," *Progress in Aerospace Sciences*, 36, 487-545.
- Miau, J.J., Lee, K.C., Chen, M.H., and Chou, J.H. "Control of a Separated Flow by a Two-Dimensional Oscillating Fence," *AIAA Journal*, 29(7):1140--1148, July 1991.
- Miau, J.J., Chen, M.H., and Chou, J.H., "Vertically Oscillating Plate Disturbing the Development of a Boundary Layer," *Journal of Fluid Mechanics*, 298:1--22, 1995.
- Miau, J.J., Chen, M.H., and Chou, J.H., "Flow Structures Behind a Vertically Oscillating Fence Immersed in a Flat-Plate Turbulent Boundary Layer," *Experiments in Fluids*, 11:118--124, 1991.
- Nelson, C.F., Koga, D.J., and Eaton, J.K., "Unsteady, Separated Flow Behind an Oscillating, Two-Dimensional Spoiler," *AIAA Journal*, 38(5):845--852, May 2000.

Personnel

Faculty

The Principal Investigators for this study are William D. Armstrong, William R. Lindberg, John McInroy, and Jonathan W. Naughton. Dr. McInroy is a faculty member in the Electrical and Computer Engineering Department at the University of Wyoming. Dr. Naughton and Dr. Lindberg are both faculty members in the Mechanical Engineering Department at the University of Wyoming. Dr. William Armstrong was a faculty member in the Department of Mechanical Engineering at the University of Wyoming until his death in August 2006.

Students

During the course of this work, several graduate students were involved.

Ezra Johnson (Mechanical Engineering Masters of Science) carried out the initial resonant actuator development and initial actuator characterization in a turbulent boundary layer flow. Mr. Johnson received his M.S. in May 2005.

Pramod Singh (Mechanical Engineering Masters of Science) carried out flow visualization experiments of an oscillating fence actuator on a flat plate in a tow tank. Mr. Singh received his M.S. in August 2006.

Paul Medina (Mechanical Engineering Masters of Science) carried out more refined characterization of the resonant actuators in a turbulent boundary layer. Mr. Medina received his M.S. in August 2006.

Seth Harvey (Electrical Engineering Doctor of Philosophy Candidate) carried out the controls work reported here.

Manjinder S. Saini (Mechanical Engineering Doctor of Philosophy Candidate) has characterized the flow to be used for evaluating the effectiveness of the sensors (oscillating airfoil) and will carry out tests in this flow with oscillating fence actuators. Mr. Saini's expected graduation date is early Fall 2007.

Michael Hind (Mechanical Engineering Masters of Science Candidate) is carrying out quantitative flow-field measurements of an oscillating fence actuator on a flat plate in a tow tank. Mr. Hind's expected graduation date is Fall 2007.

Publications

Thesis

1. Johnson, Ezra S., "Pressure Response of a Dynamically Altered Turbulent Boundary Layer," M.S. Thesis, University of Wyoming, Laramie, WY, May 2005.
2. Singh, Pramod, "Flow Visualization Studies of Flow Structures Past Static and Oscillating Solid Fences in a Flat Plate Boundary Layer," M.S. Thesis, University of Wyoming, Laramie, WY, December 2005.
3. Medina, Paul F., "Experimental Study of a Resonant Fence Actuator in a Turbulent Boundary Layer," M.S. Thesis, University of Wyoming, Laramie, WY, August 2006a.

Conference Papers

1. Saini, M.S., Lindberg, W.R., and Naughton, J.W., "Initial Studies of an Oscillating Airfoil for Characterizing Fence Actuators for Flutter Suppression," AIAA Paper 2006-0484, 44th Aerospace Sciences Meeting, Reno, NV, January 2006.
2. Medina, P.F., Lindberg, W.R. and Naughton, J.W., "Experimental Study of a Resonant Fence Actuator in a Turbulent Boundary Layer," AIAA Paper 2006-0880, 44th Aerospace Sciences Meeting, Reno, NV, January 2006b.

Journal Articles

1. Medina, P.F., Lindberg, W.R. and Naughton, J.W., "Experimental Study of a Resonant Fence Actuator in a Turbulent Boundary Layer," in preparation for submission to *Experiments in Fluids*.